Ab initio thermal transport in compound semiconductors

L. Lindsay, D. A. Broido, and T. L. Reinecke

Phys. Rev. B **87**, 165201 — Published 2 April 2013

DOI: 10.1103/PhysRevB.87.165201

Ab initio thermal transport in compound semiconductors

L. Lindsay[1], D. A. Broido[2], and T. L. Reinecke[1]

[1]Naval Research Laboratory, Washington, D.C. 20375, USA

[2]Department of Physics, Boston College, Chestnut Hill, Massachusetts 02467, USA

Abstract

We use a recently developed *ab initio* approach to calculate the lattice thermal conductivities of compound semiconductors. An exact numerical solution of the phonon Boltzmann transport equation is implemented, which uses harmonic and anharmonic interatomic force constants determined from density functional theory as inputs. We discuss the method for calculating the anharmonic interatomic force constants in some detail, and we describe their role in providing accurate thermal conductivities in a range of systems. This first-principles approach obtains good agreement with experimental results for well-characterized systems (Si, Ge, and GaAs). We determine the intrinsic upper bound to the thermal conductivities of cubic aluminum-V, gallium-V, and indium-V compounds as limited by anharmonic phonon scattering. The effects of phonon-isotope scattering on the thermal conductivities are examined in these materials and compared to available experimental data. We also obtain the lattice thermal conductivities of other technologically important materials, AlN and SiC. For most materials, good agreement with the experimental lattice thermal conductivities for naturally occurring isotopic compositions is found. We show that the overall frequency scale of the acoustic phonons and the size of the gap between acoustic and optic phonons play important roles in determining the lattice thermal

conductivity of each system. The first-principles approach used here can provide quantitative predictions of thermal transport in a wide range of systems.

PACS: 66.70.-f, 63.20.kg, 71.15.-m

I. INTRODUCTION

Semiconductor materials have played an important role in the advancement of new technologies and devices. With the growing demand for more efficient, lower-cost, reduced-size electronic devices, consideration and manipulation of the constituent material properties is essential. As devices become smaller and faster, thermal management has become an increasingly important issue. High thermal conductivities are needed for passive heat spreading, and low thermal conductivities play an important role in high efficiency thermoelectric materials. In semiconductors, around room temperature and higher, lattice vibrations (phonons) carry the majority of heat while electronic contributions to the thermal conductivity often are negligible. The lattice thermal conductivity, κ_L, is limited mainly by intrinsic phonon-phonon scattering which arises from crystal anharmonicity and from extrinsic scattering processes such as point defects and boundaries [1].

To understand rigorously how material properties determine κ_L and to devise mechanisms by which to manipulate thermal transport, accurate representation of the intrinsic phonon-phonon scattering is important. Until recent years, full microscopic descriptions of this scattering have been unavailable, and many theories of κ_L resorted to simple models involving a number of *ad hoc* approximations. Among them, the Debye approximation for phonon dispersions was often used, neglecting dispersion in the acoustic branches and ignoring optic phonons altogether, and mode averaged Gruneisen constants were often used to estimate the intrinsic phonon scattering rates [1-5]. Such approximations are of questionable validity, and because such models are typically fit to experimental data, they lack predictive power. Finally, in cases where the extrinsic scattering is not well-known these models can misrepresent the intrinsic phonon-phonon scattering when obtaining parameters from experiment.

Recently, first principles approaches based on the solution of the phonon Boltzmann transport equation (BTE) [6] have been developed, which provide accurate results for the intrinsic phonon-phonon scattering and κ_L for a number of bulk semiconductor systems and have demonstrated good agreement with measured data using no adjustable parameters [7-17]. In these approaches interatomic force constants (IFCs) that are required to calculate phonon frequencies and scattering rates are generated using density functional theory [18, 19] (DFT) and/or density functional perturbation theory (DFPT) [20]. This approach has the advantage of being predictive and can readily and accurately be applied to many materials in contrast to empirical interatomic potentials. We note that other methods such as molecular dynamics within the Green-Kubo formalism have also been developed to calculate κ_L using IFCs from DFT [21]. In some sense, the BTE and molecular dynamics approaches are complementary: The BTE directly calculates quantum mechanical scattering rates, but it includes only lowest order phonon-phonon interactions and so becomes less accurate at very high temperatures where higher order processes can become important. The molecular dynamics approach includes anharmonicity to all orders, but it is based on a classical picture and so less valid at lower temperatures. Accurate results for κ_L with molecular dynamics methods have been obtained and depend on system size and sampling methods, which can become computationally costly. Until now first principles methods have been applied to relatively few systems, including silicon (Si), germanium (Ge), and their alloys [7-8], diamond [9-11], GaAs [12], magnesium oxide (MgO) [13], half-Heusler compounds [14], lead selenide (PbSe), lead telluride (PbTe), and their alloys [15], gallium nitride (GaN) [16], magnesium silicide (Mg_2Si), magnesium stannide (Mg_2Sn), and their alloys [17]. In this paper we apply a first-principles BTE approach to determine κ_L in a range of technologically important compound semiconductors.

In Section II we briefly describe the BTE thermal transport theory and discuss details of our real-space DFT calculations for determining the anharmonic IFCs that govern phonon-phonon scattering. The calculated κ_L for the test cases, Si, Ge, and GaAs, are presented in Section III with discussion of the effects of supercell size, enforcement of symmetry conditions, and interaction radii on the anharmonic IFCs and κ_L. Results and discussion are given for aluminum-V, gallium-V, and indium-V cubic compounds in Section IV and for cubic silicon carbide (3C-SiC) and wurtzite aluminum nitride (AlN) in Section V. A summary and conclusions are given in Section VI. We compare the calculated phonon dispersions for the materials studied in this paper with available experimental data in the Appendix.

II. THERMAL TRANSPORT AND ANHARMONIC IFCS

Quantitative understanding of κ_L requires an accurate microscopic description of the intrinsic anharmonic phonon-phonon scattering. Here we briefly discuss the phonon Boltzmann transport equation approach used to determine rigorously κ_L. Details of this approach can be found in Refs. 7, 9-11, 16, 22-24. The thermal conductivity tensor is:

$$\kappa_{\alpha\beta} = \frac{1}{V}\sum_{\lambda}(\partial n_{\lambda}^{0}/\partial T)\hbar\omega_{\lambda}v_{\lambda\alpha}v_{\lambda\beta}\tau_{\lambda\alpha} \qquad (1)$$

where V is the crystal volume, α and β are Cartesian directions, n_{λ}^{0} is the Bose distribution function, $\tau_{\lambda\alpha}$ is the phonon lifetime, ω_{λ} is the phonon frequency, and $v_{\lambda\alpha} = d\omega_{\lambda}/dq_{\alpha}$ is the component of the phonon velocity in the α^{th} direction. Here, $\lambda = (\vec{q}, j)$ designates a phonon with wavevector $\vec{q}$ in branch j. For the systems examined here $\kappa_{\alpha\beta}$ is diagonal and can be described by a scalar for cubic structures and by in- and out-of-plane components for wurtzite structures [25]. The phonon frequencies are determined by diagonalization of the dynamical matrix (see the appendix).

We consider κ_L to be limited by intrinsic three-phonon scattering and by extrinsic point defect scattering by isotopic impurities. For high quality semiconductors these are the dominant scattering mechanisms for phonons above a few tens of kelvin [1]. The intrinsic anharmonic scattering rates, $1/\tau_\lambda^{anh}$, [16] are determined from scattering processes involving three phonons that satisfy conservation of energy and momentum: $\omega_\lambda \pm \omega_{\lambda'} = \omega_{\lambda''}$ and $\vec{q} \pm \vec{q}' = \vec{q}'' + \vec{K}$. The $\pm$ signs correspond to the two types of possible three-phonon processes and $\vec{K}$ is a reciprocal lattice vector, which is zero for normal (N) processes and non-zero for Umklapp (U) processes [1]. The isotope scattering rates, $1/\tau_\lambda^{iso}$, are determined from perturbation theory [26, 27]. The phonon scattering time within the single mode relaxation time approximation (RTA), $\tau_\lambda^{RTA} = [1/\tau_\lambda^{anh} + 1/\tau_\lambda^{iso}]^{-1}$, can be determined from these scattering rates alone, however, the full solution of the BTE is required to determine the actual phonon transport time, $\tau_{\lambda\alpha}$ [7, 9-11, 16, 22-24, 28-29]. Using τ_λ^{RTA} in the calculation of the thermal conductivity, κ_{RTA}, the N phonon-phonon scattering processes are incorrectly treated as resistive [1]. The full BTE solution corrects for this and therefore gives a larger κ_L. The difference between κ_L from the full solution and κ_{RTA} gives a measure of the importance of the N scattering relative to U scattering. In most of the materials considered here, the U scattering is relatively strong around room temperature, so κ_{RTA} does not differ much from the full solution to the BTE. Similar behavior has been previously noted in Si and Ge [7, 30]. For systems with very strong N scattering relative to U scattering, such as in diamond [9-11], graphene [31, 32] and carbon nanotubes [22, 33], the full solution to the BTE is required to accurately determine κ_L.

The BTE formalism requires harmonic IFCs, $\Phi_{\alpha\beta}(l\kappa, l'\kappa')$, as inputs to determine the phonon frequencies, eigenvectors, and velocities. The anharmonic IFCs, $\Phi_{\alpha\beta\gamma}(l\kappa, l'\kappa', l''\kappa'')$, are

required to determine the phonon-phonon scattering rates [7, 9-11, 16, 22-24]. All IFCs were calculated using norm-conserving pseudopotentials in the local density approximation (LDA) with the plane-wave QUANTUM ESPRESSO package [34, 35]. The ground state configuration of each system was determined by adjusting the structural lattice constants (*a* for cubic, *a* and *c* for wurtzite) to find the minimum energy [36]. The harmonic IFCs were calculated using standard DFPT. Typically, convergence was achieved with 80 Ryd plane-wave cut-offs and 6x6x6 k-point meshes for electronic and phonon calculations.

Calculation of the anharmonic IFCs is not part of typical electronic structure packages. The anharmonic IFCs used in this work were calculated using a real-space "frozen phonon" approach within DFT [16, 37]. We define a nearest neighbor cut-off radius for which interactions between atoms separated by a distance larger than the cut-off are taken to be zero. A large number of anharmonic three-phonon elements, $\Phi_{\alpha\beta\gamma}(0\kappa,l'\kappa',l''\kappa'')$, need to be determined, which can be computationally costly. Fortunately, symmetry considerations establish relationships between IFCs and limit the number of independent elements to be calculated [37-39]. We use symmetry conditions to identify a set of independent IFCs, ϕ_i, from which all anharmonic IFCs can be linearly constructed:

$$\Phi_{\alpha\beta\gamma}(l\kappa,l'\kappa',l''\kappa'') = \sum_i \phi_i \Lambda_i(l\kappa,l'\kappa',l''\kappa'') \qquad (2)$$

The sum in Eq. 2 runs over all independent anharmonic IFCs and $\Lambda_i(l\kappa,l'\kappa',l''\kappa'')$ are constants determined by the symmetry operations that establish the relationship of each ϕ_i with each anharmonic IFC. For cubic crystals there is a simple one-to-one correspondence between anharmonic IFCs giving $\Lambda_i(l\kappa,l'\kappa',l''\kappa'')=0$ for all but one element for which $\Lambda_i(l\kappa,l'\kappa',l''\kappa'')=\pm 1$. For structures with less symmetry, such as hexagonal lattices, there is not

necessarily a one-to-one correspondence between IFCs and the $\Lambda_i(l\kappa,l'\kappa',l''\kappa'')$ are not simple integers.

For each independent IFC element, pairs of atoms (one from the unit cell and one of its neighbors depending on the element) were systematically perturbed from equilibrium by a small distance within a large ground-state supercell. These supercells must be sufficiently large so that interactions with perturbed periodic supercell images do not contribute significantly to the calculations. The resulting Hellmann-Feynman forces [34] on all the atoms were calculated via Γ-point self-consistent calculations for 4 different perturbations to obtain numerical derivatives of the forces and thus the anharmonic IFC element. Since the forces for *all* of the atoms are calculated for a given perturbation, this method over-determines the independent IFC elements. We find that numerical differences between calculated elements that should be the same by symmetry are typically small and subsequently use their average.

Before applying symmetry operations to the independent IFC elements to determine the dependent IFCs, other important symmetry properties need to be considered. In particular, the truncation of anharmonic interactions to a finite number of neighbors breaks translational invariance (TI) of the crystal. Translational invariance can play an important role in determining the scattering properties of long-wavelength acoustic phonons and thus in determining κ_L. The TI conditions can be written as [17, 38]:

$$\sum_{l''\kappa''}\Phi_{\alpha\beta\gamma}(0\kappa,l'\kappa',l''\kappa'')=\sum_j\phi_j A_{ij}=B_i=0 \qquad (3)$$

Due to derivative permutation symmetry there is also a set equations for the sum over $l'\kappa'$. Each *i* represents a separate TI equation for each combination of variables that is not summed over. B_i is the sum for each TI condition that should be zero for perfect translational invariance, and we

use the more compact notation $A_{ij} = \sum_{l'\kappa' \text{ or } l''\kappa''} \Lambda_j(0\kappa, l'\kappa', l''\kappa'')$ to write Eq. 3 in terms of the independent IFCs, ϕ_i. We employed and tested three different procedures for enforcing the TI conditions: i) simple acoustic sum rule (ASR), ii) χ^2 minimization, and iii) Lagrange multipliers. For the ASR method, a subset of anharmonic IFCs are defined in terms of the others:

$$\Phi_{\alpha\beta\gamma}(0\kappa, l'\kappa', 0\kappa) = -\sum_{l''\kappa'' \neq 0\kappa} \Phi_{\alpha\beta\gamma}(0\kappa, l'\kappa', l''\kappa'') \tag{4}$$

as well as permutations. Using the ASR method has the advantage of being simple and guarantees that the TI conditions are met. However, it violates derivative permutation and point group symmetries of the system. For the second method we use a numerical algorithm [40] to minimize the function $\chi^2 = \sum_i B_i^2$ by adding a small compensation to each ϕ_i. This procedure and the Lagrange multipliers method (described in Ref. 17 and Ref. 41) change only the independent IFCs and thus maintain all symmetry properties of the crystal while enforcing the TI conditions. Given the set of independent IFCs the symmetry operations can then be used to determine all other anharmonic IFCs.

III. TEST CASES (Si, Ge, and GaAs)

Here we present calculated results for κ_L of Si, Ge, and GaAs and quantify our discussion of various aspects of the anharmonic calculations in terms of their effects on κ_L. These materials have been extensively studied and reliable measurements of κ_L for both isotopically enriched and naturally occurring isotope concentrations are available.

Figure 1 shows the calculated κ_L vs. temperature for Si. Solid curves are calculated κ_L for isotopically pure Si, κ_{pure}, and dashed curves are calculated κ_L with naturally occurring Si isotope

concentrations, $\kappa_{natural}$. Circles [42] are experimental κ_L for isotopically enriched Si and triangles [42] and squares [43-44] are experimental $\kappa_{natural}$. We note that the κ_L data from Ref. 42 agree well with the data from Ref. 45 (not shown) taken from three different laboratories. The black and red curves are for κ_L determined with anharmonic IFCs calculated in a 64 atom supercell and a 216 atom supercell, respectively. All calculations include anharmonic IFCs out to 3rd nearest neighbors and the TI conditions enforced using the χ^2 minimization procedure. The green dashed curve (lowest) is $\kappa_{natural}$ determined with anharmonic IFCs calculated in a 64 atom supercell but without enforcing the TI conditions. The red curves (216 atom supercell) show excellent agreement with the κ_L data from Ref. 42 over a wide temperature range without use of adjustable parameters. We also calculated κ_L for isotopically purified Si (99.983% ^{28}Si, 0.014% ^{29}Si, and 0.003% ^{30}Si) corresponding to experiment [42] and find negligible difference with κ_{pure} over the entire temperature range. The black curves (64 atom supercell) demonstrate good agreement with the red curves even though a much smaller supercell was used to calculate the anharmonic IFCs. The green curve for $\kappa_{natural}$ without enforcing the TI conditions on the anharmonic IFCs is significantly lower than the red and black curves and experiment. The absence of TI causes an artificial enhancement of low frequency scattering of heat-carrying acoustic phonons and thus reduces κ_L.

Figure 2 shows the calculated κ_{pure} (solid curves) and $\kappa_{natural}$ (dashed curves) for Ge with experimental values for isotopically purified Ge (circles) and with naturally occurring isotopic abundances (triangles) [46]. The red, black, and purple curves correspond to κ_L determined with translational invariance enforced via the χ^2 minimization procedure, the Lagrange multiplier method, and the simple ASR method, respectively. The green dashed curve corresponds to $\kappa_{natural}$ without TI conditions enforced on the anharmonic IFCs. As with Si, the $\kappa_{natural}$ of Ge as

calculated without enforcing the TI conditions is much less than experiment and the other calculations. The calculated $\kappa_{natural}$ using the simple ASR (purple dashed curve) to enforce TI, which results in violation of other crystal symmetries, also falls significantly below both experiment and the corresponding black and red curves. The κ_L calculated using the χ^2 minimization procedure (red curves) and the Lagrange multipliers method (black curves) are in good agreement with each other and with experiment. Figures 1 and 2 demonstrate that TI plays an important role in determining κ_L and show that as long as TI and the point group and permutation symmetries are satisfied the method for TI enforcement is not a critical issue.

We test the effects of the nearest neighbor cut-off radius on κ_L for GaAs in Figure 3. Since GaAs is a polar compound with long range Coulomb interactions the calculation of κ_L in GaAs may be more sensitive to the cut-off radius than Si or Ge. Figure 3 shows the calculated $\kappa_{natural}$ for GaAs with different nearest neighbor cut-off radii along with experimental data for $\kappa_{natural}$ (green triangles [47] and black triangles [48]) and κ_L for isotopically purified GaAs (green circles [47] and black circles [48]). The calculated curves included 2nd (green), 3rd (solid black), 4th (red), and 5th (blue) nearest neighbors for the anharmonic IFCs. The 2nd, 3rd, 4th, and 5th nearest neighbor cut-off radii were 0.75*a*, 0.85*a*, 1.05*a*, and 1.1*a*, respectively, which included interactions of unit cell atoms with 16, 28, 34, and 46 surrounding atoms, respectively. Here *a* is the lattice constant (see Table 1). We found that including only 1st nearest neighbors required very large changes to the anharmonic IFCs in order to enforce the TI conditions and thus was not included here. We have also used a reciprocal-space DFPT approach (black dashed curve) to calculate the anharmonic IFCs and to calculate $\kappa_{natural}$, which extends the interactions to 7th nearest neighbors and includes long range Coulomb interactions [7, 9-11, 49-50]. As can be seen in Figure 3, the calculated $\kappa_{natural}$ is fairly insensitive to the nearest neighbor cut-off radius. The

inset to Figure 3 gives an expanded view of the curves around room temperature. With increasing number of nearest neighbors, the magnitudes of the anharmonic IFCs obtained from both real space and DFPT approaches involving distant atoms become smaller, which provides more potential for accuracy errors. Nevertheless, the variation in the room temperature GaAs κ_L values shown for the different cases in the inset to Figure 3 is less than 4%. We find that the DFPT approach gives similar variation of κ_L for different numbers of nearest neighbors (not shown). This suggests a robustness of the first principles real space approach for κ_L presented here. All of the theoretical curves lie above the experimental data from Ref. 48 and agree somewhat better with the data from Ref. 47. We also note that κ_L of GaAs does not have much enhancement with isotopic purification, ~5% at room temperature.

We have shown through these test cases (Si, Ge, and GaAs) that calculations of κ_L are fairly insensitive to reasonable choices of supercell size and nearest neighbor cut-off distance. We have also demonstrated that it is important to enforce translational invariance conditions while maintaining the point group and derivative permutation symmetries to accurately determine κ_L.

IV. III-V CUBIC SEMICONDUCTORS

In this section we apply the first-principles approach for κ_L discussed in Sections II and tested on well-studied Si, Ge, and GaAs to the III-V cubic compound materials. For all cases, we used 216 atom supercells with an interaction cut-off to include 3rd nearest neighbors for calculating anharmonic IFCs. We enforced translational invariance via the χ^2 minimization procedure. The lattice constants used to calculate the harmonic and anharmonic IFCs were determined by energy minimization except for InP, InAs, and InSb (discussed below). For each material in this paper, the lattice constants and mass variance parameters [26] used in the calculations of κ_L and the calculated κ_{pure}, $\kappa_{natural}$, and percent isotope effect (percent increase in κ_{pure} compared to

$\kappa_{natural}$), $P = 100 \times (\kappa_{pure} / \kappa_{natural} - 1)$ are in Table 1. Also in Table 1 is the percent increase to the room temperature κ_{pure} from the full solution to the BTE compared to the RTA solution, $S = 100 \times (\kappa_{pure} / \kappa_{RTA} - 1)$. For small *S*, U phonon-phonon scattering is large and the RTA solution to the BTE is a good approximation for κ_L. For large *S*, N phonon-phonon scattering processes are important and the fully iterated solution is required to accurately give κ_L.

The calculated κ_{pure} for the different materials is limited by only three-phonon scattering and represents the intrinsic upper bound to κ_L. To compare better with experiment we also include isotopic impurity scattering to determine $\kappa_{natural}$ for systems composed of elements with differing natural isotopic abundances. We note that experimental samples may contain defects (dislocations, substitutions, other impurities, etc.). Further, at low temperatures sample size and grain boundaries can play a significant role in determining κ_L. These scattering mechanisms are not considered in this work, but they can significantly lower κ_L below the values obtained here.

Aluminum-V compounds

Here we examine κ_L of AlP, AlAs, and AlSb. Figure 4 shows calculated κ_L vs. temperature for isotopically pure AlP (solid green curve), AlAs (solid red curve), and AlSb (solid black curve). Phonon-isotope scattering is particularly important in AlSb in part due to the large isotope mixture of Sb (57.21% ^{121}Sb and 42.79% ^{123}Sb) while the isotope mixtures for Al, P, and As are negligible. Thus, the calculated $\kappa_{natural}$ is shown only for AlSb by the dashed black curve in Figure 4. The circles correspond to experimental data for $\kappa_{natural}$ of AlP (solid green [51]) and AlSb (solid black [51] and hollow black [52]). An experimental data point for κ_L of AlAs at T=300K [53] (not shown) lies directly on the solid green circle. Optic phonons play an important role in determining κ_L for all of the materials considered in this work, but especially so when comparing κ_L of the aluminum-V compounds. We note that the importance of optic

phonon scattering of heat-carrying acoustic phonons has been previously discussed in a number of papers including Refs. 11, 15, 16, 22, 28, 29, 51, and 54. In AlSb the large mass mismatch of Al and Sb atoms results in a substantial frequency gap between acoustic and optic branches (see Figure A5). Important phonon scattering processes of the type: $acoustic + acoustic \leftrightarrow optic$ (*aao*) are completely forbidden by energy conservation due to the gap in AlSb. Further, energy conservation forbids *ooo* scattering in all the materials considered here and the phase space for *aoo* scattering in AlSb is very small due to the frequency gap. These restrictions become less severe as the mass differences between Al and anions decrease and the frequency gaps decrease [51, 55] (see Figures A3-A5).

At T=100K the optic phonons are not significantly thermally populated, and so they do not provide much scattering resistance to the lower frequency acoustic phonons regardless of the frequency gap. In this temperature regime *aaa* scattering provides the dominant thermal resistance in all materials. AlP generally has the weakest *aaa* scattering of these compounds due to a higher frequency scale of the acoustic phonons, which decreases phonon populations and limits the phase space for this scattering. Further, AlP has the highest acoustic velocities. Thus, at 100K κ_{pure} for AlP is 2.2 times higher than κ_{pure} for AlSb and is the highest of the three materials. With increasing temperature anharmonic phonon scattering becomes greater and κ_L decreases, as can be seen for all the curves in Figure 4. The κ_{pure} for AlP decreases faster with increasing temperature than κ_{pure} for AlAs and AlSb due to stronger *aao* scattering in AlP as optic phonons are increasingly thermally populated. At T=300K, AlP has the lowest κ_{pure} of the three materials due to having the smallest frequency gap and thus stronger acoustic-optic scattering.

AlSb has the highest κ_L at room temperature due to the severely restricted acoustic-optic scattering compared to the other materials, which leads to both increased acoustic phonon lifetimes and increased optic phonon lifetimes. Unlike all of the other materials in this work, the phase space for three-phonon scattering of optic phonons in AlSb is so restricted that the optic modes provide significant contributions to κ_L despite having lower velocities than typical acoustic phonons. Since *aao* and *ooo* scattering channels are completely forbidden by energy conservation *aoo* scattering provides the only intrinsic resistance for optic phonons in AlSb. The phase space for *aoo* scattering is sensitive to the splitting of the longitudinal optic (LO) branch and the transverse optic (TO) branch which arises from long range Coulomb interactions. Increased LO/TO splitting leads to a larger phase space for *aoo* scattering and reduces optic phonon contributions to κ_L, while having little effect on the acoustic phonon contributions.

We note that in PbTe [15], Mg_2Si [17], and SWCNTs [22, 33] optic phonon contributions to κ_L were also found to be significant. However, in those cases the large contributions stemmed from optic branches that were relatively dispersive and resided at lower frequencies rather than from a restricted phase space for scattering. The inset to Figure 4 shows the κ_{pure} vs. temperature for AlSb (black curve) with the contributions to κ_{pure} from the acoustic phonons (red curve) and the optic phonons (green curve). For T>250K the optic modes actually provide the dominant contribution to κ_L. As the temperature decreases, the contributions to κ_L from both acoustic and optic modes increase as anharmonic scattering gets smaller, but the acoustic phonon contribution to κ_L continues to increase while the optic phonon contribution peaks at T=175K and then drops. This reflects the significant decrease in the optic phonon population with decreasing temperature due to their higher frequencies, which reduces their contributions to κ_L. The large gap in AlSb substantially weakens the U scattering compared to N scattering for the optic modes. Thus, κ_{pure}

from the full solution to the BTE is 40% higher than κ_{RTA} (see Table 1). The acoustic contributions to κ_L of AlSb only give *S*=2%, while the optic modes give *S*=116%. In contrast, the total increase is only *S*=3% for AlP.

We find good agreement with the experimental κ_L data for AlP and AlAs, however, the calculated $\kappa_{natural}$ for AlSb is ~50% above experiment at T=300K. The experimental κ_L data was taken from an AlSb sample believed to have had appreciable amounts of impurities [52]. We note that point defects can be particularly effective at scattering high frequency optical phonons. The dotted black curve in Figure 4 gives the acoustic-only contribution (assuming that additional defects eliminate the optic contributions as in typical materials) to $\kappa_{natural}$ of AlSb which is in excellent agreement with the experimental data.

Gallium-V compounds

We previously presented results for κ_L and *P* for wurtzite GaN and compared those results with the calculated *P* for GaAs, GaSb, GaP, and cubic GaN [16]. Here we give κ_L for these cubic compounds. Figure 5 shows the calculated $\kappa_{natural}$ vs. temperature for GaSb (black dashed curve), GaAs (green dashed curve), GaP (red dashed curve), and cubic GaN (blue dashed curve). Also shown are κ_{pure} for GaP (red solid curve) and cubic GaN (blue solid curve). Experimental data is shown for κ_L of GaSb (black circles [56]), GaAs (green circles [47] and green triangles [48]), and GaP (red circles [51] and red triangles [52]). For GaN the lattice constant determined by energy minimization was increased ~1% to give better agreement with the experimental phonon dispersion as discussed in Ref. 16 and discussed below for the indium-V materials. We used the lattice constants determined by energy minimization for GaAs, GaP, and GaSb, which gave good agreement for the phonon dispersions (see Figures A6-A8).

GaN has the largest frequency gap between acoustic and optic phonons and the largest acoustic frequency scale of the gallium-V materials (see Figures A6-A9). These properties give higher phonon velocities and weaker anharmonic phonon scattering in GaN and thus significantly larger κ_L than the other materials in Figure 5. κ_{pure} for GaN is over 2 times larger than κ_{pure} for GaP over the entire temperature range. We also note that the full BTE solution for κ_{pure} of GaN is 13% higher than the RTA result at T=300K. For the other materials the difference is around 5% or less (see Table 1). A disparity exists between the calculated $\kappa_{natural}$ for GaP and the experimental results from Ref. 52, the calculated result being 20% higher at room temperature. The samples studied in Ref. 52 were believed to have had appreciable amounts of impurities which may be the cause of the differences. The calculated $\kappa_{natural}$ for GaAs and GaSb are in good agreement with experiment.

Due to the large frequency gap and frequency scale in GaN, the anharmonic phonon scattering is relatively weak and phonon-isotope scattering is relatively more important for limiting κ_L than in materials with stronger phonon-phonon scattering. The isotope effect in GaN is very large, with P=68% at T=300K and increases with decreasing temperature as the anharmonic phonon scattering gets weaker. Figure 6 shows previously published [16] calculated isotope effects, P, vs. temperature for cubic GaN (solid black curve), wurtzite GaN (dashed black curve), GaP (green curve), and GaSb (orange curve) with the addition of the calculated P for diamond [11] (gold curve), Ge (red curve), AlSb (brown curve), and 3C-SiC (blue curve). The room temperature P for all the materials studied in this work are also given in Table 1. At T=300K GaN has the largest isotope effect which can be understood in terms of the large Ga isotope mixture, the large frequency gap, and the high frequency scale in GaN [16]. Though diamond has a smaller isotopic mass variance than GaN and no frequency gap between acoustic

and optic phonons it also has a large isotope effect, P=51% at T=300K. Anharmonic phonon coupling is very weak in diamond at T=300K making phonon-isotope scattering important. The weak anharmonic coupling arises from a small unit cell mass and strong covalent bonding which gives diamond a very high acoustic frequency scale, ~3.5 times higher than GaN (compare Figure A9 and Figure 1 of Ref. 9). These properties give diamond a high κ_L and P [9, 11].

Despite having a smaller isotopic mass variance and relatively small frequency scale (roughly half that of GaN), AlSb has P=36% at T=300K. The large isotope effect and its temperature dependence are a consequence of significant optic phonon contributions to κ_L discussed above. The weak anharmonic scattering leads to significantly increased optic phonon lifetimes and larger contributions to κ_{pure} compared to other materials. The isotope scattering rates scale roughly as $\omega^2 D(\omega)$ [26] where $D(\omega)$ is the phonon density of states which is large for the relatively flat optic branches. Thus, isotope scattering strongly suppresses the optic phonon contributions to $\kappa_{natural}$ leading to a large percentage isotope effect, P. Unlike the other curves in Figure 6, the P for AlSb has a peak at 175K and decreases with decreasing temperature below the peak. As the temperature decreases below the peak, the optic phonons become less thermally populated and contribute less to κ_L than the acoustic phonons despite weakening anharmonic scattering. Since the acoustic phonons have lower frequencies and are less affected by the isotope scattering than the optic phonons, P is reduced.

Indium-V compounds

As discussed in Section III, the LDA approach to calculate the harmonic and anharmonic IFCs tends to overbind atoms [57], and corrections for zero-point and non-zero temperature atomic motion [58] account for only a small fraction of the difference. For most of the systems examined in this work excellent agreement with the experimental phonon dispersions (see

figures in the Appendix) is achieved in spite of this underestimation of the lattice constants. However, like previous work calculating phonon dispersions and κ_L of GaN, we find the calculated optic phonon frequencies for InP, InAs, and InSb are higher than the experimental dispersion leading to artificially weakened acoustic-optic phonon scattering.

Energy minimization gives lattice constants a_{InP}=5.79Å, a_{InAs}=5.97Å, and a_{InSb}=6.39Å while measured values are 1.43%, 1.53%, and 1.40% higher, respectively. Further, the optic phonon branches given by these lattice constants (red curves in Figures A10-A12) lie above the experimental phonon dispersions. The black curves in these figures correspond to the calculated phonon dispersions using lattice constants that were increased by 1.5% for InP and 1.0% for InAs and InSb. Similar to GaN, the increased lattice constants for the indium-V systems lower the high-lying optic phonon branches and give better agreement with the experimental data. The calculated $\kappa_{natural}$ given by the different lattice constants for each indium-V compound are compared in Figure 7.

Figure 7 shows the calculated κ_L vs. temperature for the indium-V compounds with experimental data for InP (black circles [59], squares [60], diamond [61], and triangle [62]), InAs (red circles [63], squares [64], diamond [65], and triangles [66]), and InSb (blue circles [56], squares [67], and triangles [68]). The isotope effect is small in the indium-V compounds so we show only the calculated $\kappa_{natural}$ in Figure 7. The dashed black curve corresponds to $\kappa_{natural}$ for InP with harmonic and anharmonic IFCs determined using the lattice constant from minimization of energy, a_{InP}=5.79Å. The solid black curve corresponds to $\kappa_{natural}$ for InP using the corrected lattice constant, a_{InP}=5.87Å. The calculated $\kappa_{natural}$ of InAs is given by the dashed (a_{InAs}=5.97Å (energy minimization)) and solid (a_{InAs}=6.03Å (corrected)) red curves and $\kappa_{natural}$ of InSb is given by dashed (a_{InSb}=6.39Å (energy minimization)) and solid (a_{InSb}=6.45Å (corrected)) blue curves.

For all indium-V compounds the $\kappa_{natural}$ given by the corrected lattice constants (solid curves) lie below the $\kappa_{natural}$ given by the lattice constants determined by energy minimization (dashed curves). With the increased lattice constants the higher lying optic modes are shifted to lower frequencies which provide stronger scattering channels for the heat-carrying acoustic phonons and thus reduced κ_L. At T=300K $\kappa_{natural}$ determined by the corrected lattice constants are 3%, 8%, and 5% lower in InP, InAs, and InSb, respectively, which gives somewhat better agreement with experiment. In general, the calculated $\kappa_{natural}$ for InSb is in good agreement with experiment. The calculated $\kappa_{natural}$ for InAs is higher than experiment throughout the temperature range suggesting that a crystal with fewer defects could lead to modest improvements in κ_L. $\kappa_{natural}$ for InP is in agreement with the experimental data point at T=300K given in Reference 62 but is higher than the other experimental data throughout the temperature range. We also note that the RTA solution to the BTE is a good approximation in the indium-V compounds and gives κ_{RTA} only a few percent below the full BTE solution.

κ_L in the compound semiconductors depends critically on the anharmonic three-phonon scattering rates determined from perturbation theory:

$$\Gamma^{(\pm)}_{\lambda\lambda'\lambda''} = \frac{\hbar\pi}{4N_0\omega_\lambda\omega_{\lambda'}\omega_{\lambda''}} \begin{Bmatrix} n^0_{\lambda'} - n^0_{\lambda''} \\ n^0_{\lambda'} + n^0_{\lambda''} + 1 \end{Bmatrix} \left|\Phi^{(\pm)}_{\lambda,\pm\lambda',-\lambda''}\right|^2 \delta(\omega_\lambda \pm \omega_{\lambda'} - \omega_{\lambda''}) \qquad (5)$$

N_0 is the number of unit cells in the crystal and the $\pm$ signs correspond to the two types of possible three-phonon processes that satisfy conservation of crystal momentum and conservation of energy [1]. The top term in the brackets is for the + process, and the bottom term for the $-$ process. The scattering matrix elements, $\Phi^{(\pm)}_{\lambda\pm\lambda'-\lambda''}$, depend on the lowest order anharmonic IFCs, $\Phi_{\alpha\beta\gamma}(l\kappa, l'\kappa', l''\kappa'')$. We note that the three-phonon scattering rates depend on both harmonic and anharmonic properties of each system. Stiff interatomic bonding in systems such as

diamond, SiC, AlN and GaN not only give large acoustic phonon velocities and high frequency scales, but also larger anharmonic IFCs. Of all the systems we have considered, diamond has the largest κ_L *and* the largest anharmonic IFCs, which tend to increase the three-phonon scattering rates. However, the higher overall phonon frequencies of diamond enter the denominator of Eq. 5 and counteract the effects of the larger anharmonic IFCs to give lower scattering rates. Conversely, InSb has lower overall phonon frequencies, has generally smaller anharmonic IFCs, and has the lowest κ_L of the compound systems. Further, the intrinsic phonon transport lifetimes also depend on the phase space for allowed scattering processes given by the conservation conditions and the coupling of non-equilibrium phonon modes through the BTE.

V. SILICON CARBIDE AND ALUMINUM NITRIDE

Here we apply the first-principles BTE approach to calculating κ_L for technologically important semiconductors, cubic 3C-SiC and wurtzite AlN. To determine the anharmonic IFCs for AlN we used a 108 atom supercell with an interaction cut-off to include 4th nearest neighbors similar to that used previously for GaN [16]. For cubic SiC we used 216 atom supercells with an interaction cut-off to include 3rd nearest neighbors, similar to the cubic compounds discussed above. For each system we enforced translational invariance via the χ^2 minimization procedure. Figure 8 shows the calculated κ_{pure} (solid black curve) and $\kappa_{natural}$ (dashed black curve) for 3C-SiC compared with experimental data given by circles [69]. The calculated in-plane and out-of-plane (c-axis) κ_{pure} for AlN are given by the red and green curves, respectively. Open green circles are the experimental κ_L along the c-axis for AlN [70]. The isotope mixtures for Al and N are negligible so we do not give $\kappa_{natural}$ for AlN.

Light atomic masses and stiff atomic bonds for the Si and C atoms give SiC large acoustic phonon velocities and a high phonon frequency scale, though significantly smaller than those of

diamond. The relatively large Si to C mass ratio produces an appreciable frequency gap between acoustic and optic branches as seen in Figure A13. These properties make SiC a high κ_L material with calculated $\kappa_{natural}$=480Wm^{-1}K^{-1} and κ_{pure}=570Wm^{-1}K^{-1} and a percentage isotope effect of *P*=20% at 300K. We note that κ_{pure} of cubic SiC is still six times smaller than that of diamond. AlN is also a relatively high κ_L material with calculated κ_{pure}=322Wm^{-1}K^{-1} at T=300K. For each system the calculated κ_L gives good agreement with the experimental data around and above room temperature. At lower temperatures where scattering from defects and boundaries becomes more important each calculated κ_L is predictably higher than experiment.

We found previously that the wurtzite and cubic GaN structures have κ_L that are similar and larger than the thermal conductivities of the cubic GaX compounds (X=P, As, and Sb) [16]. Similarly, wurtzite AlN has significantly higher κ_L than the cubic AlX compounds discussed in the previous section (see Table 1). AlN has the largest acoustic phonon frequency scale and the highest acoustic velocities of all the AlX materials. Thus, at 100K the in-plane κ_{pure} of AlN is the largest of these materials, over five times larger than that of AlP. AlN does not have an appreciable gap between the acoustic and optic branches (see Fig. A14), and thus with increasing temperature the κ_L of AlN decreases rapidly as *aao* scattering becomes stronger. At 300K κ_{pure} is still more than 2.5 times larger than that for the cubic AlX compounds. The decay of optic phonons into the heat-carrying acoustic phonons was previously shown to increase κ_L in AlN [54]. Similarly, we find that the coupling of different phonon modes through the full solution to the BTE plays a significant role in determining κ_L of AlN. The single mode relaxation time approximation gives κ_{RTA} of AlN 14% smaller than that given by the full BTE solution.

VI. SUMMARY AND CONCLUSIONS

We have presented an accurate and predictive first-principles method for calculating the lattice thermal conductivity, κ_L, for a range of semiconducting systems. This method uses harmonic and anharmonic interatomic forces from density functional theory calculations as inputs to the linearized phonon Boltzmann transport equation for which an exact numerical solution is obtained. The calculations of the anharmonic force constants and their role in determining the thermal conductivities of a variety of systems was discussed. This first principles approach was tested on well-studied systems (Si, Ge, and GaAs) and excellent agreement with measured κ_L data was found. We used this approach to examine κ_L in aluminum-V, gallium-V, and indium-V compounds as well as the technologically important materials, SiC and AlN. The upper bound to the intrinsic κ_L as limited by anharmonic phonon scattering was calculated for each system, and the role of isotope scattering was examined. The interplay between harmonic and anharmonic crystal properties in determining the intrinsic phonon-phonon scattering rates was also discussed.

In general, the calculated $\kappa_{natural}$ is in good agreement with the available experimental data for most materials. For some compounds such as GaP, AlSb, InAs, and InP the calculated $\kappa_{natural}$ lies above the measured data suggesting that improved crystal growth to reduce point defects and other extrinsic scattering mechanisms could lead to enhancements in κ_L. We have found high intrinsic κ_L values for 3C-SiC, AlN, and cubic GaN ranging from around 300-600$Wm^{-1}K^{-1}$ at T=300K, while cubic GaN and AlSb showed large isotope effects. The frequency gap between acoustic and optic phonons plays an important role in reducing the acoustic-optic phonon scattering and in determining κ_L for compounds with large mass differences between the cations and the anions. A large acoustic-optic frequency gap in AlSb leads to significant optic phonon contributions to κ_L and to a large calculated isotope effect.

The microscopic, first-principles method presented in this work is a powerful tool for calculating and examining κ_L which is predictive and transferable to a wide range of systems.

ACKNOWLEDGMENTS

This work was supported in part by ONR and DARPA (L.L. and T.L.R.). L.L. acknowledges a NRC/NRL Research Associateship. D.A.B acknowledges support from the National Science Foundation under Grant No. 1066634 and from the S3TEC, an Energy Frontier Research Center funded by the US Department of Energy, Office of Science, Office of Basic Energy Sciences under Award No. DE-FG02-09ER46577. We also thank Wu Li, Natalio Mingo, and Derek Stewart for useful discussions.

APPENDIX

Given a set of harmonic IFCs, $\Phi_{\alpha\beta}(l\kappa,l'\kappa')$, the phonon frequencies are determined by diagonalization of the dynamical matrix:

$$D_{\alpha\beta}^{\kappa\kappa'}(\vec{q}) = \frac{1}{\sqrt{\overline{m}_{\kappa}\overline{m}_{\kappa'}}} \sum_{l'} \Phi_{\alpha\beta}(0\kappa,l'\kappa') e^{i\vec{q}\cdot\vec{R}_{l'}} \tag{A1}$$

for a given wavevector, $\vec{q}$. Here, $\overline{m}_{\kappa}$ is the isotope averaged mass of the κ^{th} atom, $\vec{R}_l$ is the lattice vector locating the l^{th} unit cell, and α and β are Cartesian directions. The harmonic IFCs for each system were calculated within the framework of DFPT and LDA using the plane-wave QUANTUM ESPRESSO package [34, 35]. For most cases we used norm-conserving pseudopotentials with 80 Ryd plane-wave cut-offs and 6x6x6 Monkhorst-Pack k-point meshes for electronic and phonon calculations. All calculations were made with pseudopotentials from the QUANTUM ESPRESSO website [34] and the names are given in the figure captions.

Here we give the phonon dispersions in the high-symmetry directions for all of the materials considered in this work. Available experimental data is included for comparison with the calculated curves.

References

[1] J. M. Ziman, *Electrons and Phonons* (Oxford University Press, London, 1960).

[2] P. G. Klemens, *Solid State Phys.* **7**, 1 (1958).

[3] J. Callaway, *Phys. Rev.* **113**, 1046 (1958).

[4] M. G. Holland, *Phys. Rev.* **132**, 2461 (1963).

[5] P. G. Klemens, *J. Wide Bandgap Mater.* **7**, 332 (2000).

[6] R. E. Peierls, *Quantum Theory of Solids* (Oxford University Press, London, 1955).

[7] D. A. Broido, M. Malorny, G. Birner, N. Mingo, and D. A. Stewart, *Appl. Phys. Lett.* **91**, 231922 (2007).

[8] J. Garg, N. Bonini, B. Kozinsky, and N. Marzari, *Phys. Rev. Lett.* **106**, 045901 (2011).

[9] A. Ward, D. A. Broido, D. A. Stewart, and G. Deinzer, *Phys. Rev. B* **80**, 125203 (2009).

[10] Wu Li, N. Mingo, L. Lindsay, D. A. Broido, D. A. Stewart, and N. A. Katcho, *Phys. Rev. B* **85**, 195436 (2012).

[11] D. A. Broido, L. Lindsay, and A. Ward, *Phys. Rev. B* **86**, 115203 (2012).

[12] T. Luo, J. Garg, J. Shiomi, K. Esfarjani, and G. Chen, arXiv:1209.6350 [cond-mat.mtrl-sci] (2012).

[13] X. Tang and J. Dong, *Proc. Natl. Acad. Sci.* USA **107**, 4539 (2010).

[14] J. Shiomi, K. Esfarjani, and G. Chen, *Phys. Rev. B* **84**, 104302 (2011).

[15] Z. Tian, J. Garg, K. Esfarjani, T. Shiga, J. Shiomi, and G. Chen, *Phys. Rev. B* **85**, 184303 (2012).

[16] L. Lindsay, D. A. Broido, and T. L. Reinecke, *Phys. Rev. Lett.* **109**, 095901 (2012).

[17] Wu Li, L. Lindsay, D. A. Broido, D. A. Stewart, and N. Mingo, *Phys. Rev. B* **86**, 174307 (2012).

[18] P. Hohenberg and W. Kohn, *Phys. Rev.* **136**, B864 (1964).

[19] W. Kohn and L. J. Sham, *Phys. Rev.* **140**, A1133 (1965).

[20] S. Baroni, S. Gironcoli, A. D. Corso, and P. Giannozzi, *Rev. of Mod. Phys.* **73**, 515 (2001).

[21] K. Esfarjani, G. Chen, and H. T. Stokes, *Phys. Rev. B* **84**, 085204 (2011).

[22] L. Lindsay, D. A. Broido, and N. Mingo, *Phys. Rev. B* **82**, 161402(R) (2010).

[23] L. Lindsay, D. A. Broido, and N. Mingo, *Phys. Rev. B* **83**, 235428 (2011).

[24] L. Lindsay and D. A. Broido, *Phys. Rev. B* **85**, 035436 (2012).

[25] We note that κ_L of wurtzite GaN and AlN have small in-plane anisotropies of around a few percent around room temperature and higher. We define $\kappa_{in} = (\kappa_{xx} + \kappa_{yy})/2$ where the hexagonal plane lies in the x-y plane and the c-axis is along the z direction.

[26] S. I. Tamura, *Phys. Rev. B* **30**, 849 (1984).

[27] A list of the mass variance parameters for naturally occurring isotope abundances of the materials studied in this work is found in Table I.

[28] M. Omini and A. Sparavigna, Phys. Rev. B **53**, 9064 (1996).

[29] M. Omini and A. Sparavigna, Nuovo Cimento Soc. Ital. Fis., D **19**, 1537 (1997).

[30] A. Ward and D. A. Broido, *Phys. Rev. B* **81**, 085205 (2010).

[31] J. H. Seol, I. Jo, A. L. Moore, L. Lindsay, Z. H. Aitken, M. T. Pettes, X. Li, Z. Yao, R. Huang, D. A. Broido, N. Mingo, R. S. Ruoff, and L. Shi, *Science* **328**, 213 (2010).

[32] L. Lindsay, D. A. Broido, and N. Mingo, *Phys. Rev. B* **82**, 115427 (2010).

[33] L. Lindsay, D. A. Broido, and N. Mingo, *Phys. Rev. B* **80**, 125407 (2009).

[34] S. Baroni *et al*, http://www.quantum-espresso.org.

[35] P. Gianozzi *et al*, *J. Phys.: Cond. Mat.* 21, 395502 (2009).

[36] For the wurtzite structures the internal parameter, *u*, which defines the relative position of the two hexagonal close-packed sublattices, was chosen so that the Hellmann-Feynman forces on the atoms were negligible.

[37] K. Esfarjani and H. T. Stokes, *Phys. Rev. B* **77**, 144112 (2008).

[38] G. Leibfried and W. Ludwig, *Solid State Phys.* **12**, 275 (1961).

[39] G. P. Srivastava, *The Physics of Phonons* (Taylor and Francis Group, LLC, New York, 1990).

[40] W. H. Press, S. A. Teukolsky, W. T. Vetterling, and B. P. Flannery, *Numerical Recipes in Fortran* (Cambridge University Press, Cambridge, 1992).

[41] N. Mingo, D. A. Stewart, D. A. Broido, and D. Srivastava, *Phys. Rev. B* **77**, 033418 (2008).

[42] A. V. Inyushkin, A. N. Taldenkov, A. M. Gibin, A. V. Gusev, and H.-J. Pohl, *Phys. Status Solidi C* **1**, 2995 (2004).

[43] T. Ruf, R. W. Henn, M. Asen-Palmer, E. Gmelin, M. Cardona, H.-J. Pohl, G. G. Devyatych, and P. G. Sennikov, *Solid State Comm.* **115**, 243 (2000).

[44] We note that κ_L of isotopically enriched Si was also reported in Ref. 43 (not shown here), however, the room temperature values were different from measurements reported in Ref. 45 on the same sample: T. Ruf, R. W. Henn, M. Asen-Palmer, E. Gmelin, M. Cardona, H.-J. Pohl, G. G. Devyatych, and P. G. Sennikov, *Solid State Comm.* **127**, 257 (2003).

[45] R. K. Kremer, K. Graf, M. Cardona, G. G. Devyatykh, A. V. Gusev, A. M. Gibin, A. V. Inyushkin, A. N. Taldenkov, and H.-J. Pohl, *Solid State Comm.* **131**, 499 (2004).

[46] V. I. Ozhogin, A. V. Inyushkin, A. N. Taldenkov, A. V. Tikhomirov, G. E. Popov, E. Haller, and K. Itoh, *JETP Lett.* **63**, 490 (1996).

[47] R. O. Carlson, G. A. Slack, and S. J. Silverman, *J. Appl. Phys.* **36**, 505 (1965).

[48] A. V. Inyushkin, A. N. Taldenkov, A. Y. Yakubovsky, A. V. Markov, L. Moreno-Garsia, and B. N. Sharonov, *Semicond. Sci. Technol.* **18**, 685 (2003).

[49] G. Deinzer, G. Birner, and D. Strauch, *Phys. Rev. B* **67**, 144304 (2003).

[50] G. Deinzer, M. Schmitt, A. P. Mayer, and D. Strauch, *Phys. Rev. B* **69**, 014304 (2004).

[51] E. F. Steigmeier and I. Kudman, *Phys. Rev.* **141**, 767 (1966).

[52] V. M. Muzhdaba, A. Y. Nashel'skii, P. V. Tamarin, and S. S. Shalyt, *Sov. Phys. Solid State* **10**, 2265 (1969).

[53] M. A. Afromowitz, *J. Appl. Phys.* **44**, 1292 (1973).

[54] M. Kazan, S. Pereira, and M. R. Correia, *Phys. Rev. B* **77**, 180302(R) (2008).

[55] L. Lindsay and D. A. Broido, *J. Phys.: Cond. Mat.* **20**, 165209 (2008).

[56] M. G. Holland, *Phys. Rev.* **134**, A471 (1964).

[57] P. Haas, F. Tran, and P. Blaha, *Phys. Rev. B* **79**, 085104 (2009).

[58] P. B. Allen, *Phil. Mag. B* **70**, 527 (1994).

[59] S. A. Aliev, A. Ya. Nashel'skii, and S. S. Shalyt, *Sov. Phys. Solid State* 7, 1287 (1965).

[60] S. Adachi, *Properties and Applications of Indium Phosphide*, EMIS Datareviews Series No. 21, edited by T. P. Pearsall (INSPEC, London, 2000).

[61] I. Kudman and E. F. Steigmeier, *Phys. Rev.* **133**, A1665 (1964).

[62] W. Both, V. Gottschalch, and G. Wagner, *Cryst. Res. Tech.* **21**, K85 (1986).

[63] P. V. Tamarin and S. S. Shaylt, *Sov. Phys. Semicond* **5**, 1097 (1971).

[64] G. Le Guillou and H. J. Albany, *Phys. Rev. B* **5**, 2301 (1972).

[65] D. G. Arasly, R. N. Ragimov, and M. I. Alief, *Sov. Phys. Semicond.* **24**, 225 (1990).

[66] R. Bowers, J. E. Bauerle, and A. J. Cornish, *J. Appl. Phys.* **30**, 1050 (1959).

[67] S. S. Shalyt, P. V. Tamarin, and V. S. Ivleva, *Phys. Lett.* **32A**, 29(1970).

[68] P. D. Maycock, *Sol. State Commun.* **10**, 161 (1967).

[69] D. T. Morelli, J. P. Heremans, and G. A. Slack, *Phys. Rev. B* **66**, 195304 (2002).

[70] G. A. Slack, R. A. Tanzilli, R. O. Pohl, and J. W. Vandersande, *J. Phys. Chem. Solids* **48**, 641 (1987).

[71] G. Nilsson and G. Nelin, *Phys. Rev. B* **6**, 3777 (1972).

[72] A. Onton, *Proc. on the 10th Int. Conf. Phys. Semicond.*, Editors: S. P. Keller, J. C. Hensel, and F. Stern (U.S. Atomic Energy Commission, New York, 1970).

[73] T. Azuhata, T. Sota, and K. Suzuki, *J. Phys.: Cond. Mat.* **7**, 1949 (1995).

[74] D. Strauch, B. Dorner, and K. Karch, *Proc. 3rd Int. Conf. On Phonon Phys.*, Editors: S. Hunklinger, W. Ludwig, and G. Weiss (World Scientific, Singapore, 1990).

[75] P. H. Borcherds, K. Kunc, G. F. Alfreys, and R. L. Hall, *J. Phys. C* **12**, 4699 (1979).

[76] D. Strauch and B. Dorner, *J. Phys.: Cond. Mat.* **2**, 1457 (1990).

[77] M. K. Farr, J. G. Traylor, and S. K. Sinha, *Phys. Rev. B* **11**, 1587 (1975).

[78] P. H. Borcherds, G. F. Alfrey, D. H. Saunderson, and A. D. B. Woods, *J. Phys. C: Solid State* **8**, 2022 (1975).

[79] N. S. Orlova, *Phys. Status Solidi B* **119**, 541 (1983).

[80] R. Carles, N. Saint-Cricq, J. B. Renucci, M. A. Renucci, and A. Zwick, *Phys. Rev. B* **22**, 4804 (1980).

[81] D. L. Price, J. M. Rowe, and R. M. Nicklow, *Phys. Rev. B* **3**, 1268 (1971).

[82] D. W. Feldman, J. H. Parker, Jr., W. J. Choyke, and L. Patrick, *Phys. Rev.* **173**, 787 (1968).

[83] M. Schwoerer-Böhning, A. T. Macrander, M. Pabst, and P. Pavone, *Phys. Stat. Sol. (b)* **215**, 177 (1999).

Table I. Experimental and calculated lattice constants determined by energy minimization, mass variance parameters, κ_{pure}, $\kappa_{natural}$, and percent isotope effect (P) at T=300K for materials considered in this work. Also included is a comparison of the room temperature κ_{pure} determined by the BTE and the thermal conductivity determined by the RTA, κ_{RTA}, for each material. The difference is given by $S = 100 \times (\kappa_{pure} / \kappa_{RTA} - 1)$.

	a_{calc} (a_{exp}) (Å)	g_{cation} (g_{anion}) ($\times 10^{-4}$)	κ_{pure} ($Wm^{-1}K^{-1}$)	$\kappa_{natural}$ ($Wm^{-1}K^{-1}$)	P	S
Diamond[a]	3.53 (3.57)	0.75 (0.75)	3450	2290	51	50
Si	5.37 (5.43)	2.01 (2.01)	155	144	8	2.4
Ge	5.61 (5.65)	5.87 (5.87)	74	60	23	6.9
3C-SiC	4.34 (4.36)	2.01 (0.75)	572	479	20	6.7
AlP	5.40 (5.45)	□ (□)	90	□	□	3.0
AlAs	5.61 (5.66)	□ (□)	105	□	□	0.5
AlSb	6.10 (6.14)	□ (0.66)	118	86	36	39
c-GaN[b]	4.42 (4.50)	1.97 (□)	362	215	68	13
GaP[c]	5.34 (5.45)	1.97 (□)	153	131	16	4.8
GaAs[c]	5.55 (5.65)	1.97 (□)	56	54	4	5.6
GaSb[c]	6.00 (6.10)	1.97 (0.66)	48	45	6	3.1
InP[b]	5.79 (5.87)	0.12 (□)	91	89	2	2.4
InAs[b]	5.97 (6.06)	0.12 (□)	36	36	.5	2.8
InSb[b]	6.39 (6.48)	0.12 (0.66)	20	20	2	3.9
w-GaN[b,d]	3.13 (3.19) 5.10 (5.19)[e] .377 (.377)[f]	1.97 (□)	401 (385)[g]	242 (239)[g]	66	7.2
w-AlN	3.05 (3.11) 4.81 (4.98)[e]	□ (□)	322 (303)[g]	□	□	14

.387 (.382)[f]

---

[a]Calculated in Reference 11.

[b]These calculated lattice constants determined by energy minimization were increased to better fit the phonon dispersions when calculating κ_L for these systems as explained in the text.

[c]The κ_L and *P* values presented here slightly differ from the calculated results from Ref. 16 which used ~0.2% increase to the lattice constants to account for zero-point and finite temperature atomic motion.

[d]Calculated in Reference 16.

[e]Calculated and experimental lattice constant, *c*, for the wurtzite structure.

[f]Calculated and experimental internal parameter, *u*, for the wurtzite structure.

[g]Out-of-plane component to κ_L along c-axis.

Table I

Figure Captions

Figure 1 Calculated κ_L vs. temperature for Si with experimental data for isotopically enriched Si (circles [42]) and for naturally occurring Si concentrations (triangles [42] and squares [43-44]). Solid curves correspond to calculated κ_{pure} and dashed curves correspond to $\kappa_{natural}$. κ_L was determined with anharmonic IFCs calculated in a 64 atom supercell (black curves) and a 216 atom supercell (red curves). The calculated $\kappa_{natural}$ for a 64 atom supercell without enforcing TI is given by the green dashed curve.

Figure 2 Calculated κ_L vs. temperature for Ge with experimental data for isotopically enriched Ge (circles) and for naturally occurring Ge concentrations (triangles) [46]. κ_L was determined with TI enforced via the χ^2 minimization procedure (red curves), the Lagrange multiplier method (black curves), and the simple ASR method (purple curves). κ_{pure} is given by solid curves and $\kappa_{natural}$ is given by dashed curves. The green dashed curve corresponds to $\kappa_{natural}$ without TI conditions enforced.

Figure 3 Calculated $\kappa_{natural}$ vs. temperature for GaAs with experimental data for isotopically enriched GaAs (green circles [47] and black circles [48]) and for naturally occurring Ga concentrations (green triangles [47] and black triangles [48]). The calculated curves included 2^{nd} (green), 3^{rd} (solid black), 4^{th} (red), and 5^{th} (blue) nearest neighbors for determining the anharmonic IFCs. The dashed black curve gives $\kappa_{natural}$ for GaAs using IFCs determined from DFPT to 7^{th} nearest neighbors and with long range Coulomb interactions included (described in text).

Figure 4 Calculated κ_{pure} vs. temperature for AlP (solid green curve), AlAs (solid red curve), and AlSb (solid black curve). Experimental data for κ_L of AlP are solid green circles [51] and for κ_L of AlSb are solid [51] and hollow [52] black circles. An experimental data point for κ_L of AlAs at T=300K [53] (not shown) lies directly on the solid green circle. Calculated $\kappa_{natural}$ for AlSb is given by the dashed black curve. The acoustic-only contribution to $\kappa_{natural}$ for AlSb is given by the dotted black curve. The inset gives κ_{pure} (black curve), the acoustic contribution to κ_{pure} (red curve), and the optic contribution to κ_{pure} (green curve) vs. temperature for AlSb.

Figure 5 Calculated κ_L vs. temperature for GaSb (black curve), GaAs (green curve), GaP (red curves), and cubic GaN (blue curves). The solid curves give κ_{pure} and the dashed curves give $\kappa_{natural}$. Experimental data is shown for κ_L of GaSb (black circles [56]), GaAs (green circles [47] and green triangles [48]), and GaP (red circles [51] and red triangles [52]).

Figure 6 Calculated isotope effect, *P*, vs. temperature for cubic GaN (solid black curve), wurtzite GaN (dashed black curve), GaP (green curve), GaSb (orange curve), diamond (gold curve), Ge (red curve), AlSb (brown curve), and 3C-SiC (blue curve).

Figure 7 Calculated κ_L vs. temperature for the indium-V compounds with experimental data for InP (black circles [59], squares [60], diamond [61], and triangle [62]), InAs (red circles [63], squares [64], diamond [65], and triangles [66]), and InSb (blue circles [56], squares [67], and triangles [68]). The dashed black curve corresponds to $\kappa_{natural}$ for InP with harmonic and anharmonic IFCs determined using the lattice constant from energy minimization, a_{InP}=5.79Å. The solid black curve corresponds to $\kappa_{natural}$ using the temperature-altered lattice constant,

a_{InP}=5.87Å. Calculated $\kappa_{natural}$ of InAs is given by the dashed (a_{InAs}=5.97Å (energy minimization)) and solid (a_{InAs}=6.03Å (corrected)) red curves and $\kappa_{natural}$ of InSb is given by dashed (a_{InSb}=6.39Å (energy minimization)) and solid (a_{InSb}=6.45Å (corrected)) blue curves.

Figure 8 Calculated κ_{pure} (solid black curve) and $\kappa_{natural}$ (dashed black curve) for 3C-SiC with experimental data given by circles [69]. The calculated in-plane and out-of-plane (c-axis) κ_{pure} for AlN are given by the red and green curves, respectively, with experimental data for c-axis κ_L [70].

Figure A1 Calculated phonon dispersion for Si in the indicated high symmetry directions (black curves). The pseudopotential used in the LDA/DFPT calculation was Si.pz-vbc.UPF [34]. Experimental data are given by black circles [71].

Figure A2 Calculated phonon dispersion for Ge in the high symmetry directions (black curves). The pseudopotential used in the LDA/DFPT calculation was Ge.pz-bhs.UPF [34]. Experimental data are given by black circles [71].

Figure A3 Calculated phonon dispersion for AlP in the high symmetry directions (black curves). The pseudopotentials used in the LDA/DFPT calculation were Al.pz-vbc.UPF and P.pz-bhs.UPF [34]. Experimental data are given by black circles [72].

Figure A4 Calculated phonon dispersion for AlAs in the high symmetry directions (black curves). The pseudopotentials used in the LDA/DFPT calculation were Al.pz-vbc.UPF and As.pz-bhs.UPF [34]. Experimental data are given by black circles [73].

Figure A5 Calculated phonon dispersion for AlSb in the high symmetry directions (black curves). The pseudopotentials used in the LDA/DFPT calculation were Al.pz-vbc.UPF and Sb.pz-bhs.UPF [34]. Experimental data are given by black circles [74].

Figure A6 Calculated phonon dispersion for GaP in the high symmetry directions (black curves). The pseudopotentials used in the LDA/DFPT calculation were Ga.pz-bhs.UPF and P.pz-bhs.UPF [34]. Experimental data are given by black circles [75].

Figure A7 Calculated phonon dispersion for GaAs in the high symmetry directions (black curves). The pseudopotentials used in the LDA/DFPT calculation were Ga.pz-bhs.UPF and As.pz-bhs.UPF [34]. Experimental data are given by black circles [76].

Figure A8 Calculated phonon dispersion for GaSb in the high symmetry directions (black curves). The pseudopotentials used in the LDA/DFPT calculation were Ga.pz-bhs.UPF and Sb.pz-bhs.UPF [34]. Experimental data are given by black circles [77].

Figure A9 Calculated phonon dispersion for cubic GaN in the high symmetry directions (black curves). The pseudopotentials used in the LDA/DFPT calculation were Ga.pz-bhs.UPF and

N.pz-vbc.UPF [34]. We note that the calculated dispersion was obtained using a 1% increase to the lattice constant from energy minimization as discussed in Ref. 16.

Figure A10 Calculated phonon dispersion for InP in the high symmetry directions. Red curves give dispersion using lattice constant determined by energy minimization and black curves give dispersion using this lattice constant with a 1.5% increase. The pseudopotentials used in the LDA/DFPT calculation were In.pz-n-bhs.UPF and P.pz-bhs.UPF [34]. We note that the indium pseudopotential included a core correction. Experimental data are given by black circles [78].

Figure A11 Calculated phonon dispersion for InAs in the high symmetry directions. Red curves give dispersion using lattice constant determined by energy minimization and black curves give dispersion using this lattice constant with a 1% increase. The pseudopotentials used in the LDA/DFPT calculation were In.pz-n-bhs.UPF and As.pz-bhs.UPF [34]. We note that the indium pseudopotential included a core correction. Experimental data are given by black circles [79] and black squares [80].

Figure A12 Calculated phonon dispersion for InSb in the high symmetry directions. Red curves give dispersion using lattice constant determined by energy minimization and black curves give dispersion using this lattice constant with a 1% increase. The pseudopotentials used in the LDA/DFPT calculation were In.pz-n-bhs.UPF and Sb.pz-bhs.UPF [34]. We note that the indium pseudopotential included a core correction. Experimental data are given by black circles [81].

Figure A13 Calculated phonon dispersion for cubic 3C-SiC in the high symmetry directions (black curves). The pseudopotentials used in the LDA/DFPT calculation were Si.pz-vbc.UPF and C.pz-vbc.UPF [34]. Experimental data are given by black circles [82].

Figure A14 Calculated phonon dispersion for wurtzite AlN in the high symmetry directions (black curves). The pseudopotentials used in the LDA/DFPT calculation were Al.pz-vbc.UPF and N.pz-vbc.UPF [34]. Experimental data are given by black circles [83].

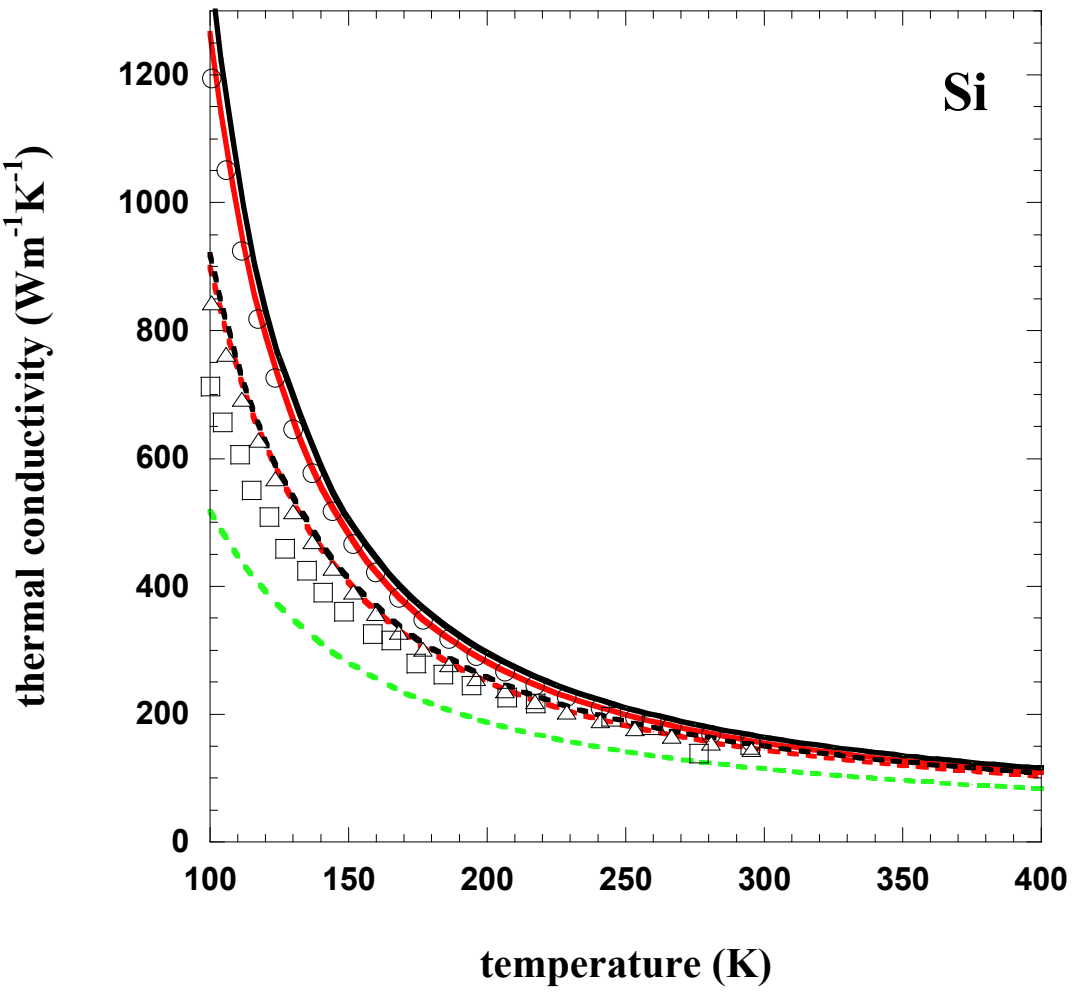
Si
thermal conductivity (Wm^{-1}K^{-1})
temperature (K)
0
200
400
600
800
1000
1200
100
150
200
250
300
350
400

Figure 1

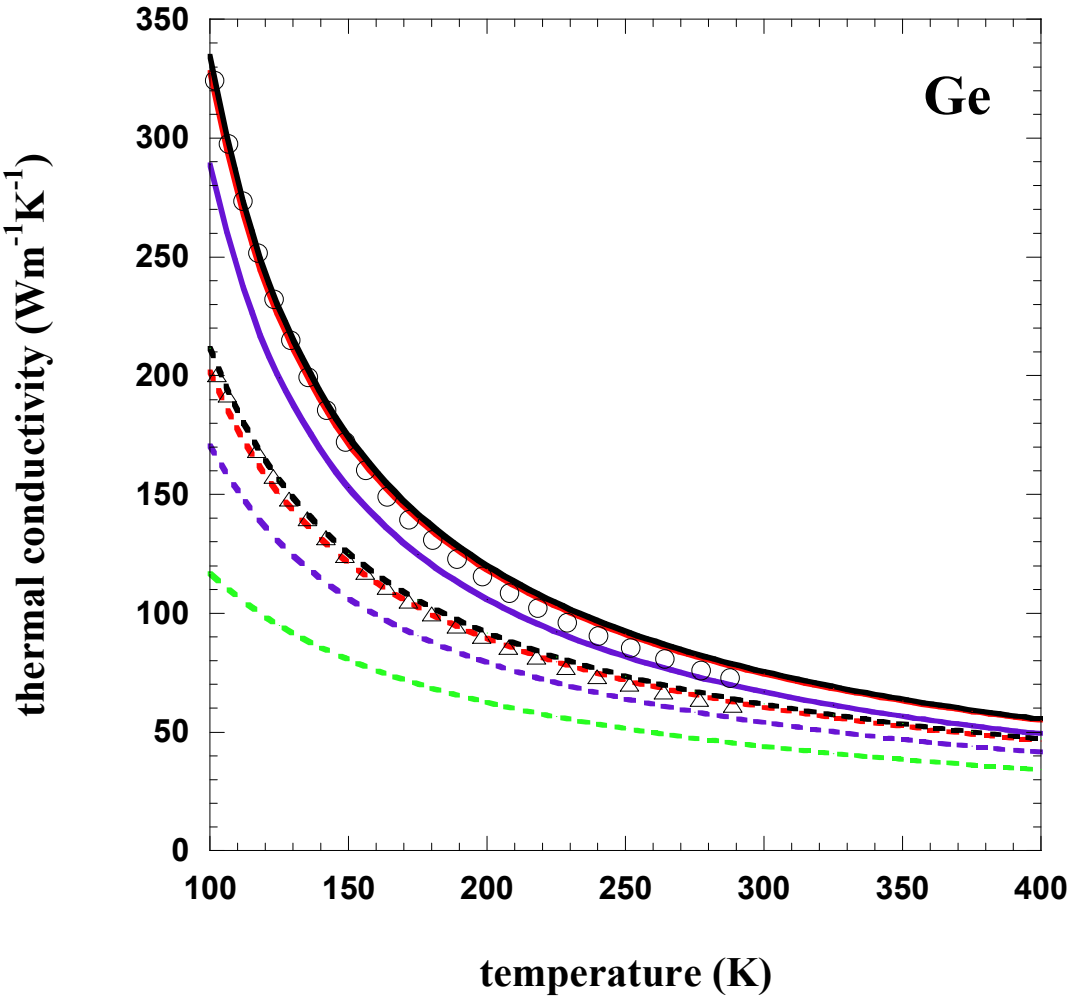
Ge
thermal conductivity (Wm^{-1}K^{-1})
temperature (K)
350
300
250
200
150
100
50
0
100
150
200
250
300
350
400

Figure 2

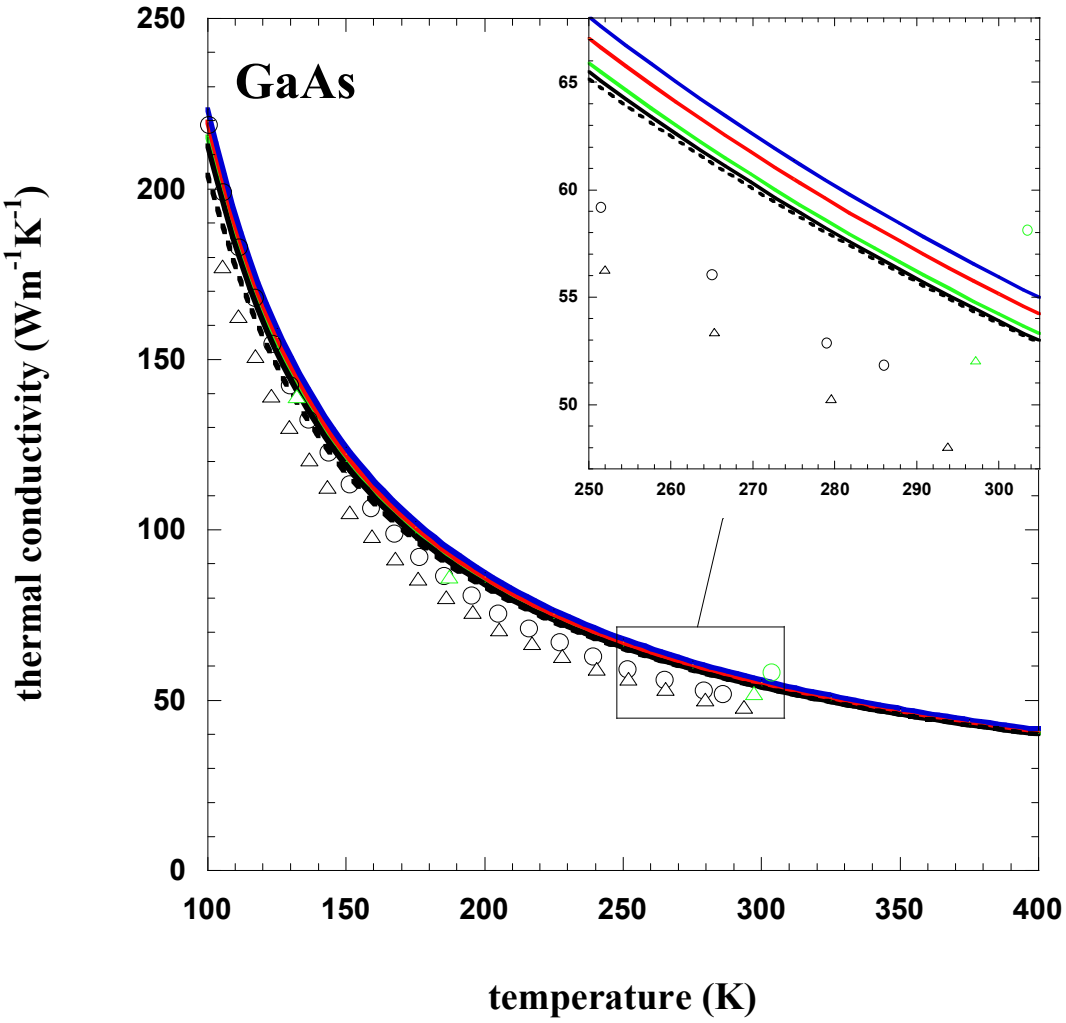
GaAs
thermal conductivity (Wm^{-1}K^{-1})
temperature (K)
250
200
150
100
50
0
100
150
200
250
300
350
400
65
60
55
50
250
260
270
280
290
300

Figure 3

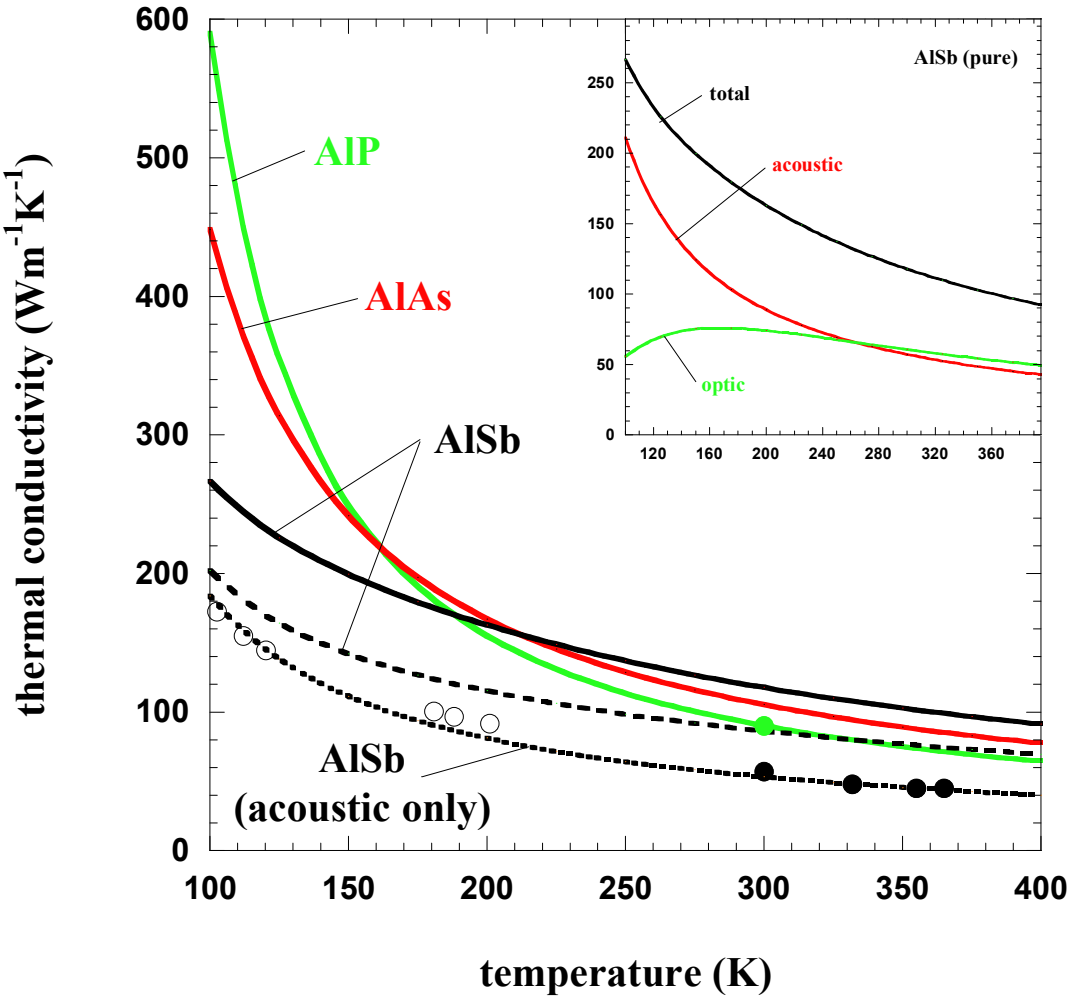
thermal conductivity (Wm^{-1}K^{-1})
temperature (K)
AlP
AlAs
AlSb
AlSb
(acoustic only)
AlSb (pure)
total
acoustic
optic

Figure 4

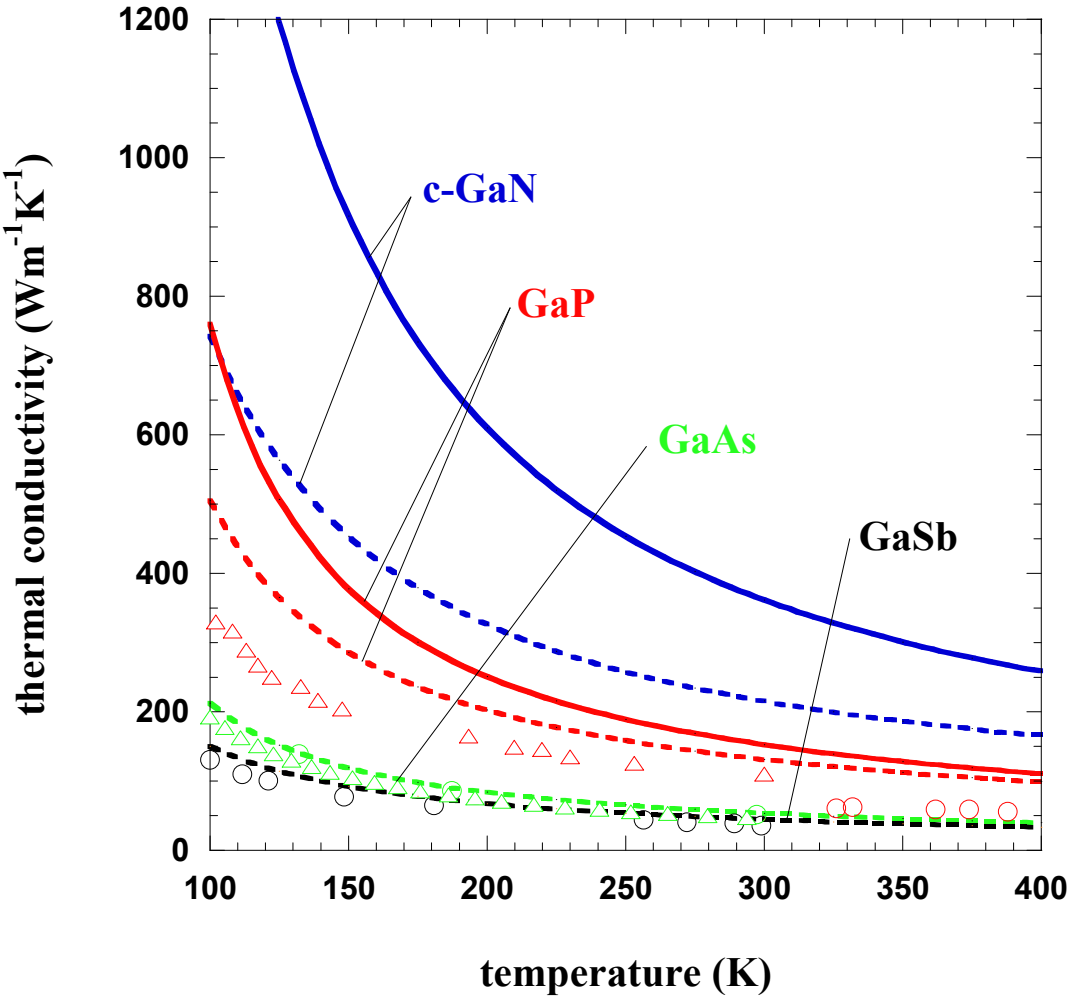
thermal conductivity (Wm-1K-1)
temperature (K)
c-GaN
GaP
GaAs
GaSb
1200
1000
800
600
400
200
0
100
150
200
250
300
350
400

Figure 5

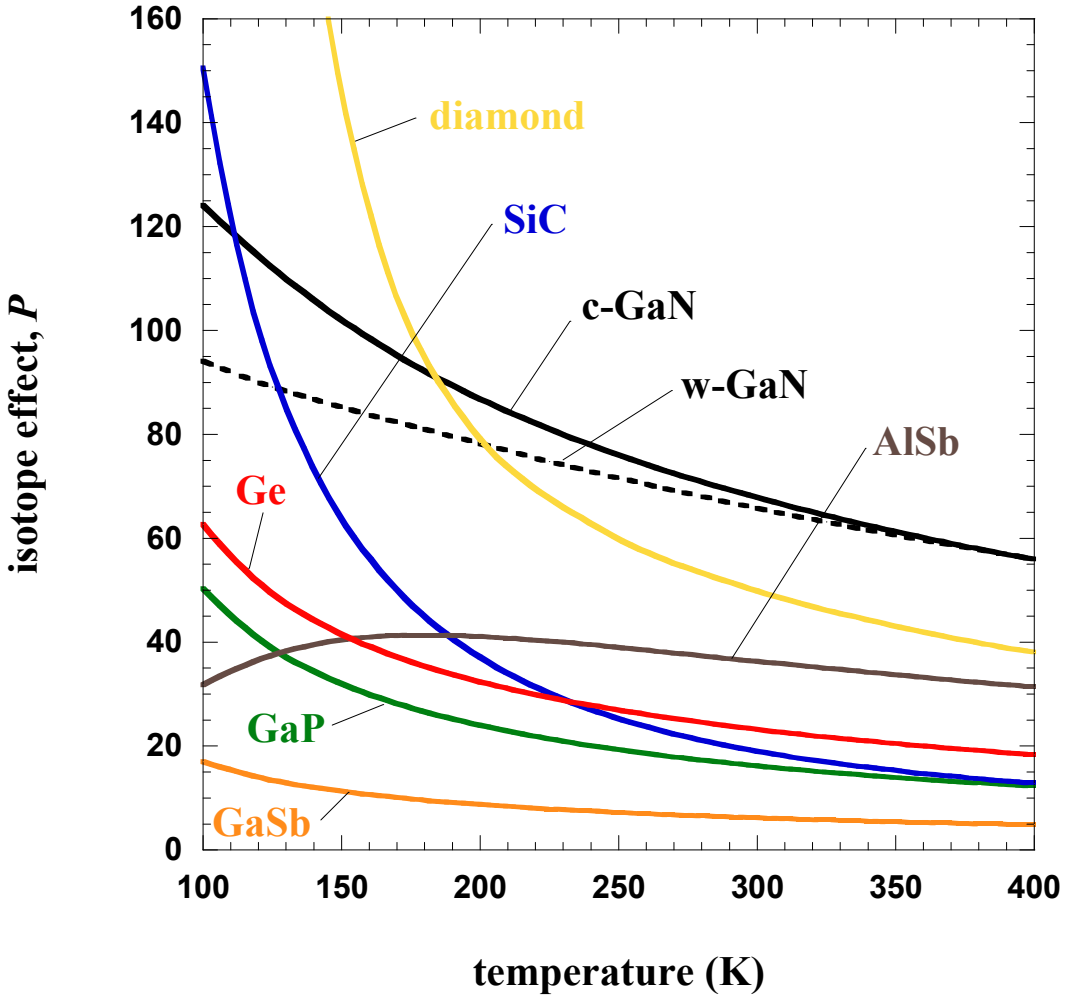
isotope effect, P
temperature (K)
diamond
SiC
c-GaN
w-GaN
AlSb
Ge
GaP
GaSb
160
140
120
100
80
60
40
20
0
100
150
200
250
300
350
400

Figure 6

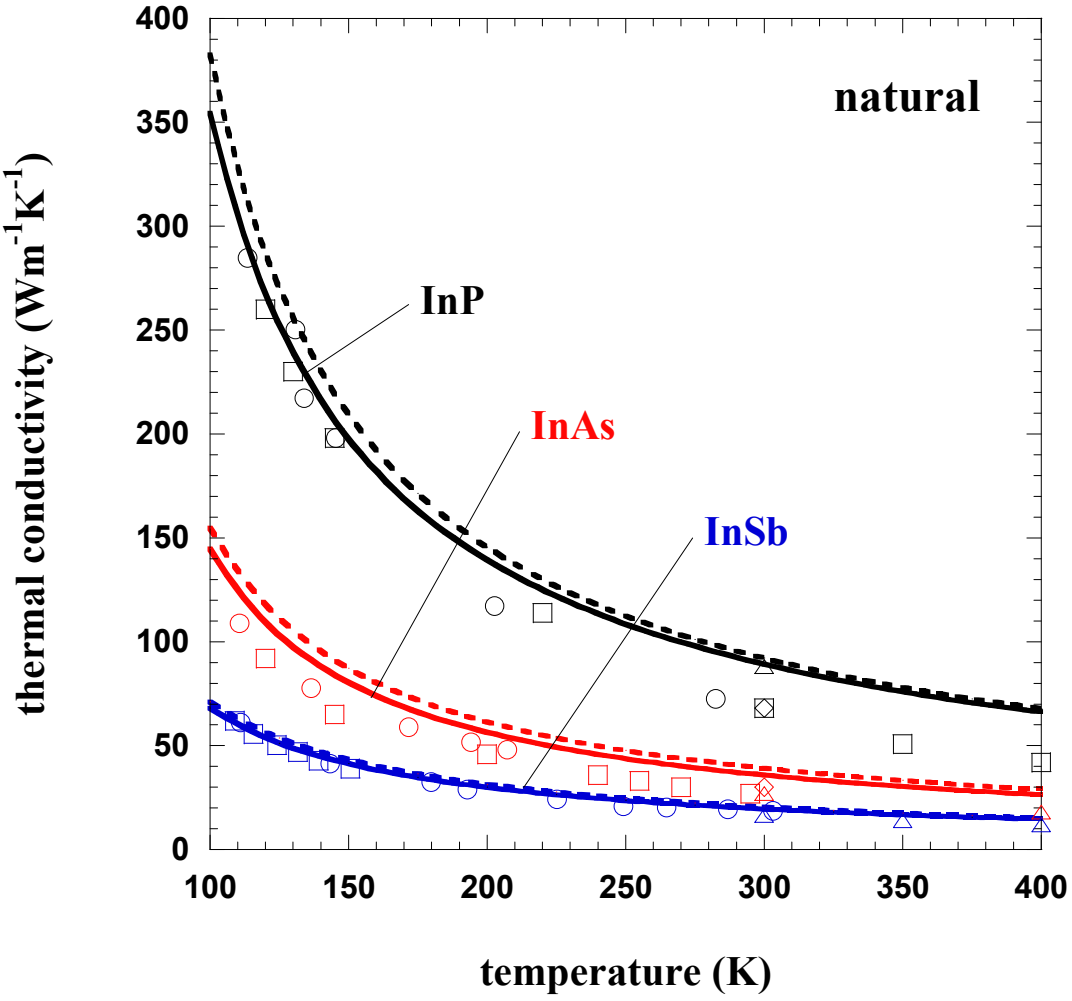
natural
InP
InAs
InSb
thermal conductivity (Wm-1K-1)
temperature (K)
0
50
100
150
200
250
300
350
400
100
150
200
250
300
350
400

Figure 7

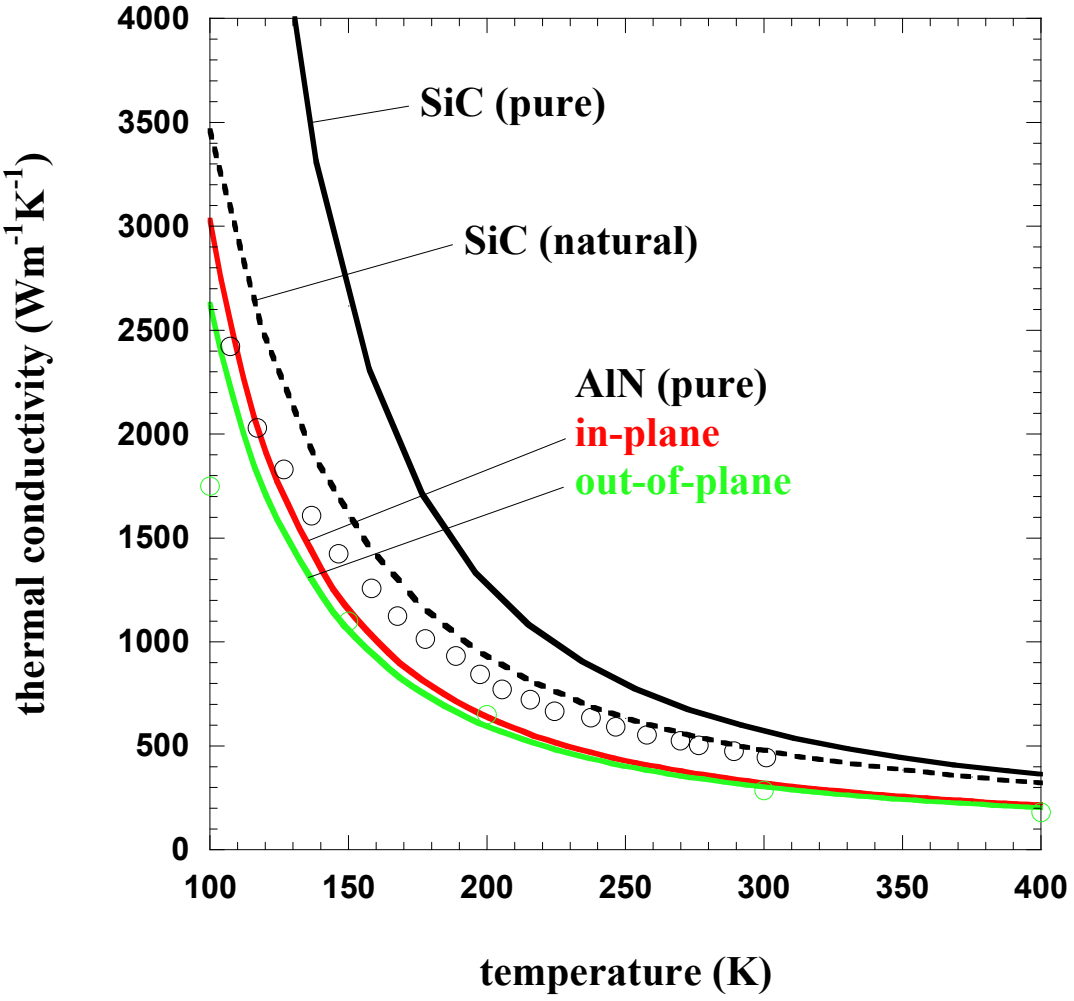
4000
3500
3000
2500
2000
1500
1000
500
0
100
150
200
250
300
350
400
thermal conductivity (Wm-1K-1)
temperature (K)
SiC (pure)
SiC (natural)
AlN (pure)
in-plane
out-of-plane

Figure 8

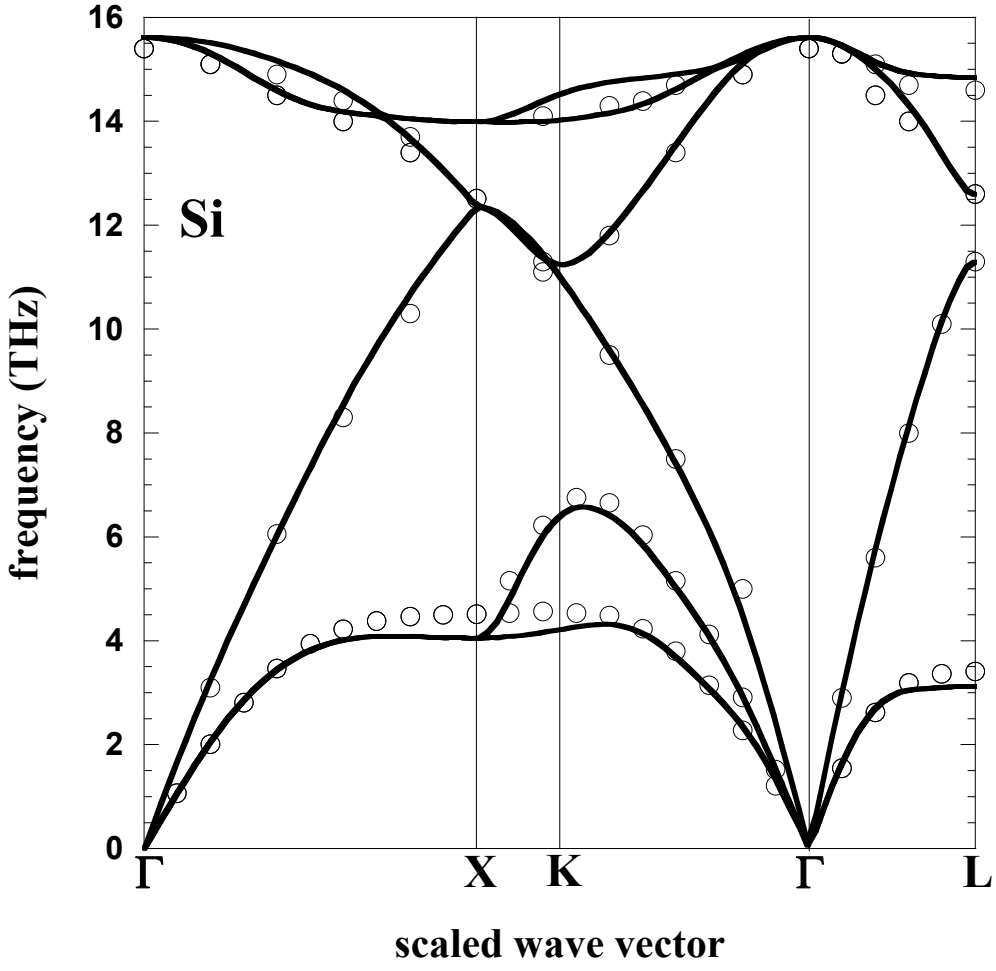

Figure A1

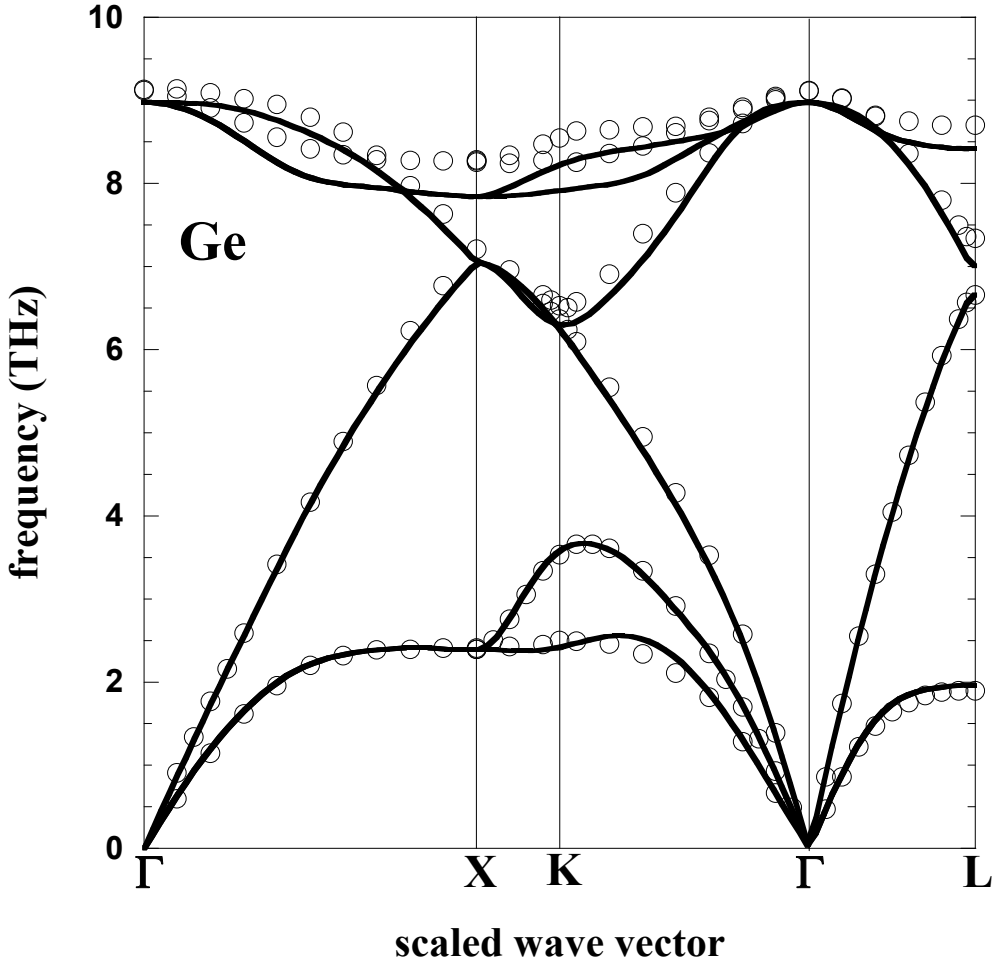

Figure A2

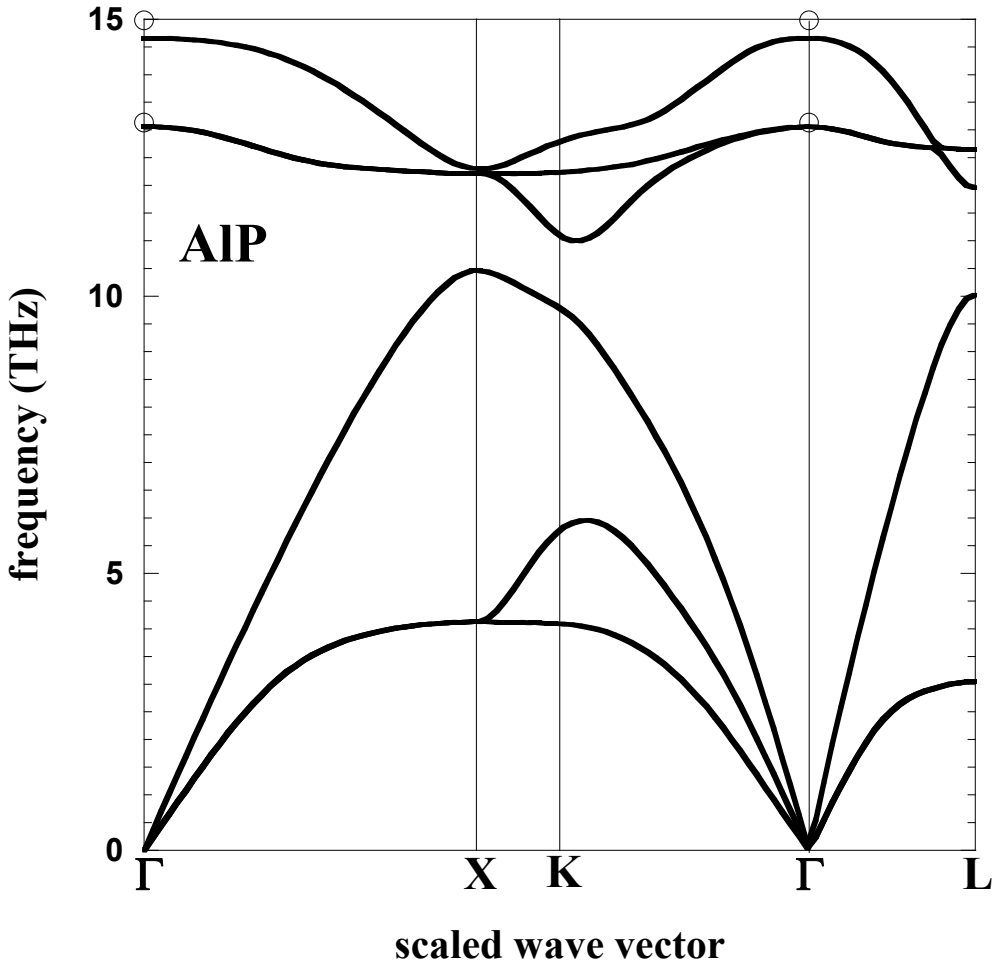

Figure A3

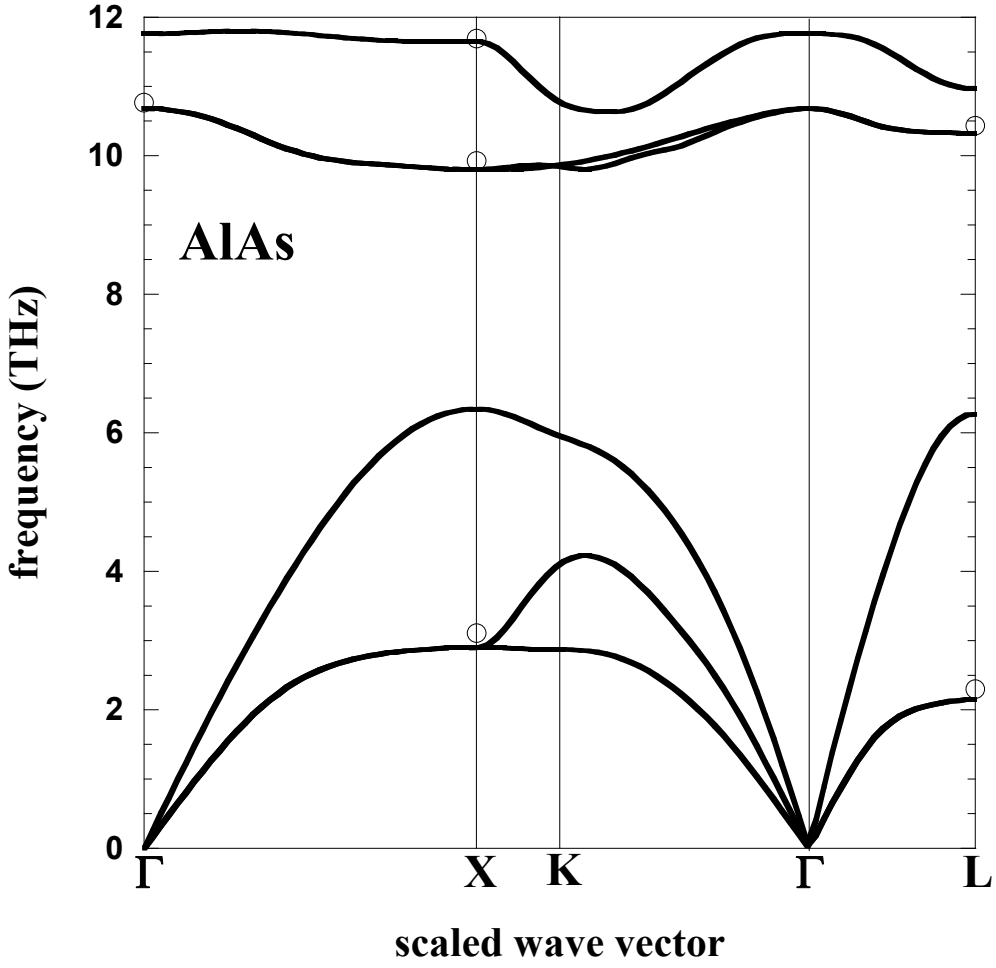

Figure A4

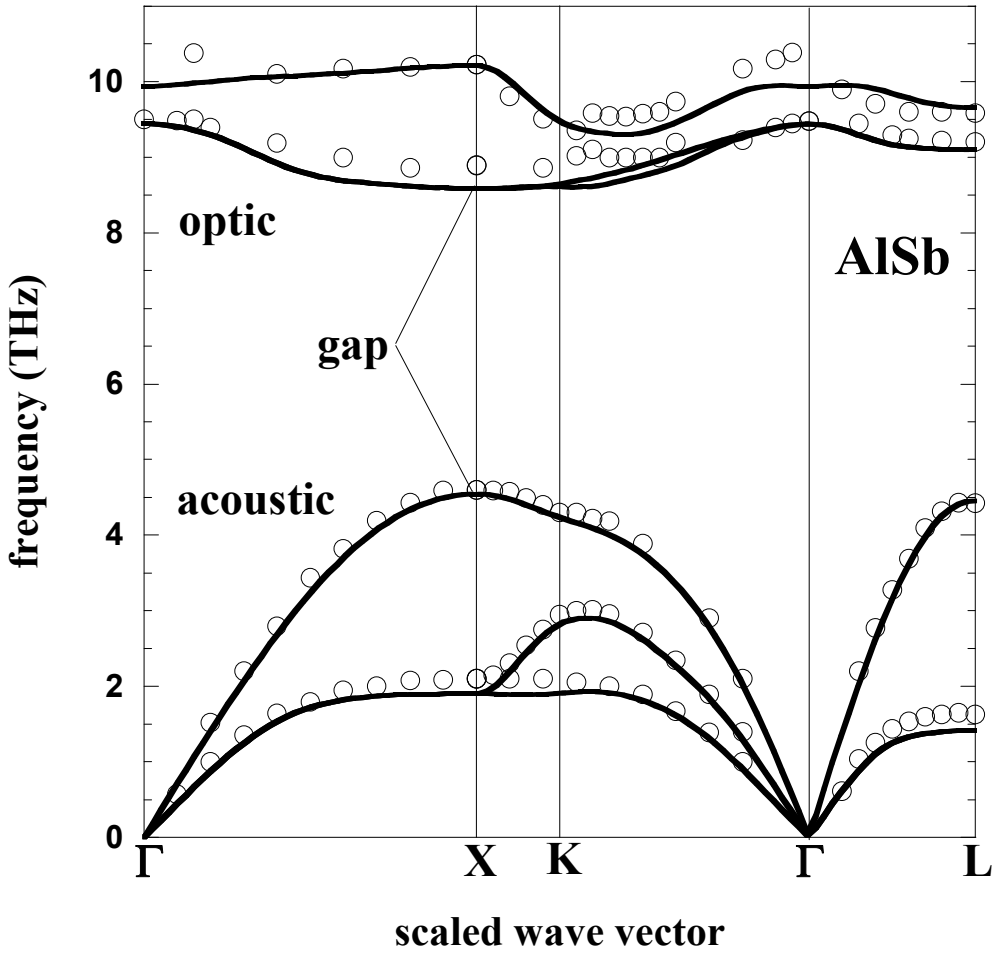
10
8
6
4
2
0
optic
AlSb
gap
acoustic
frequency (THz)
Γ
X
K
Γ
L
scaled wave vector

Figure A5

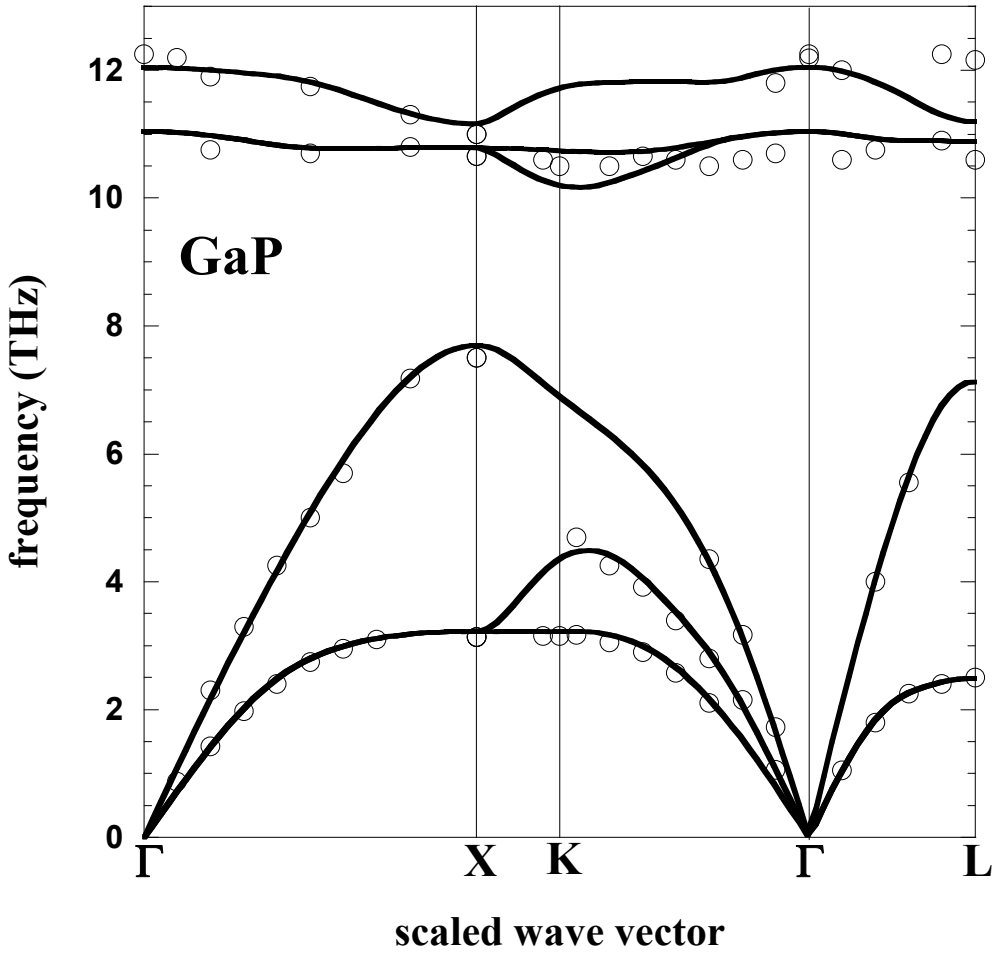

Figure A6

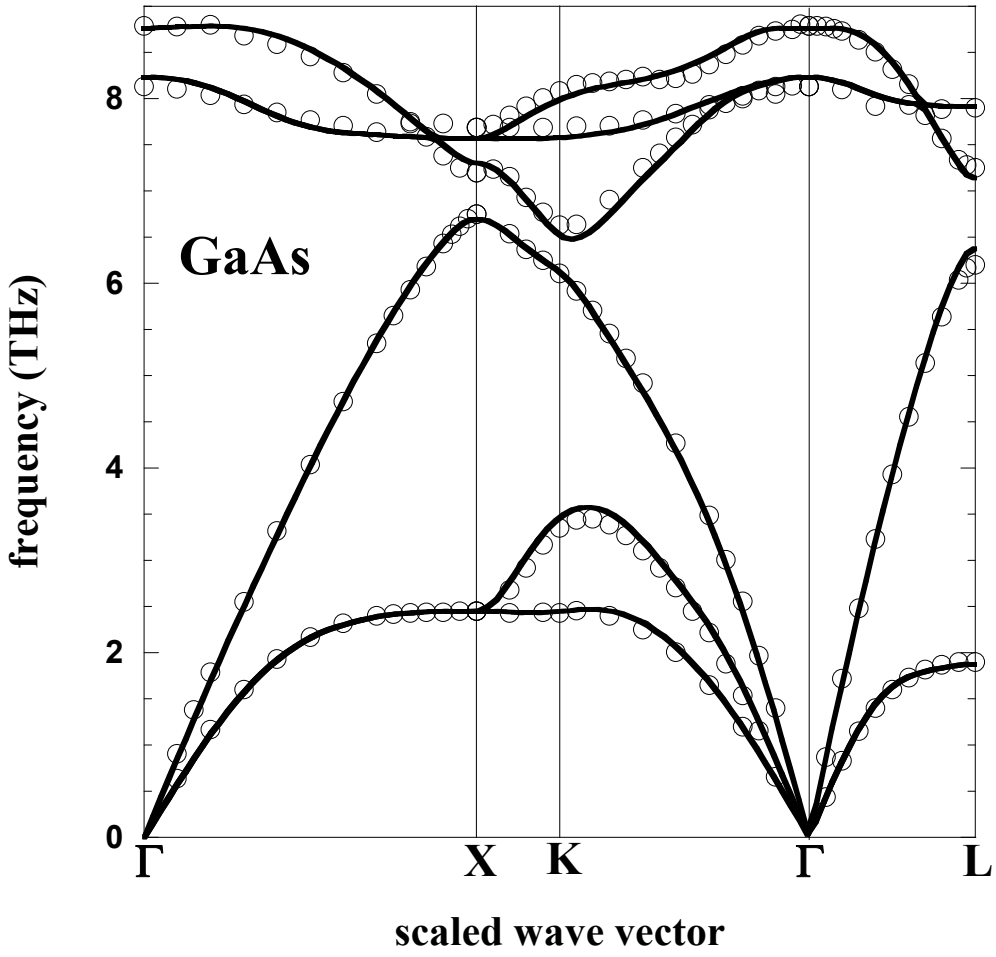

Figure A7

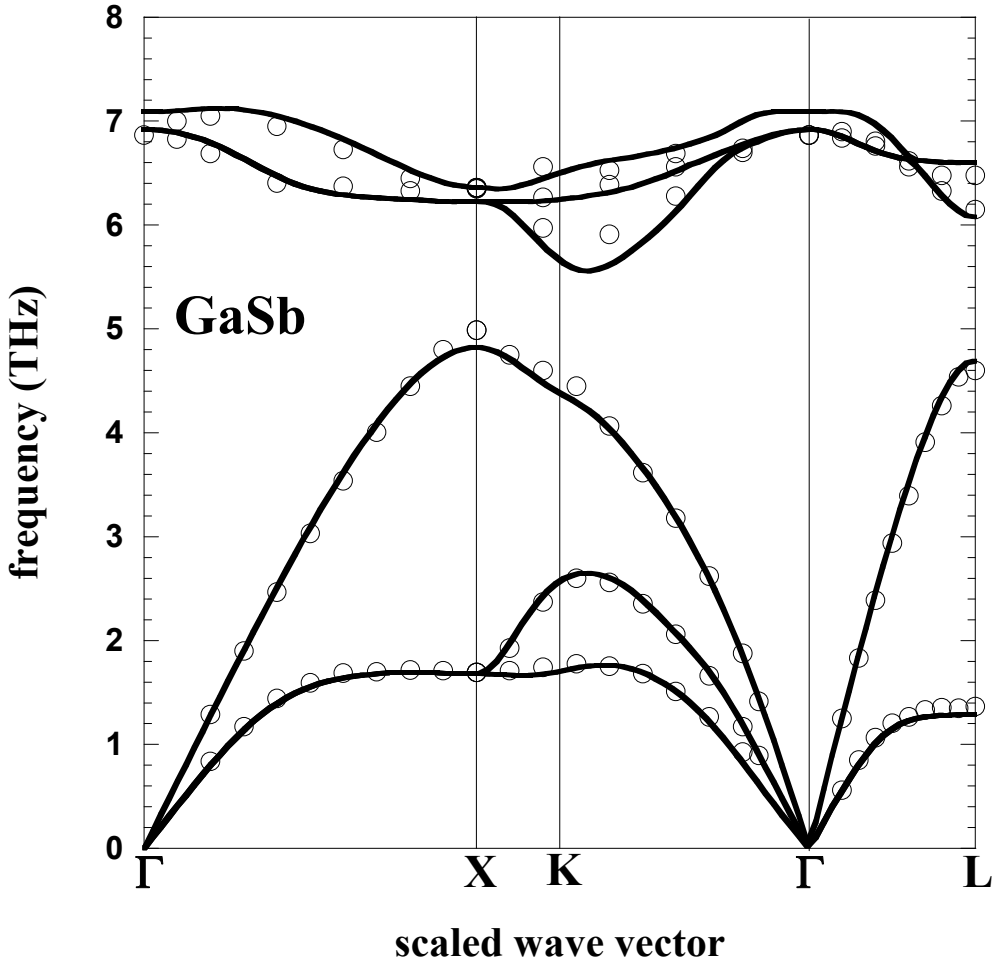

Figure A8

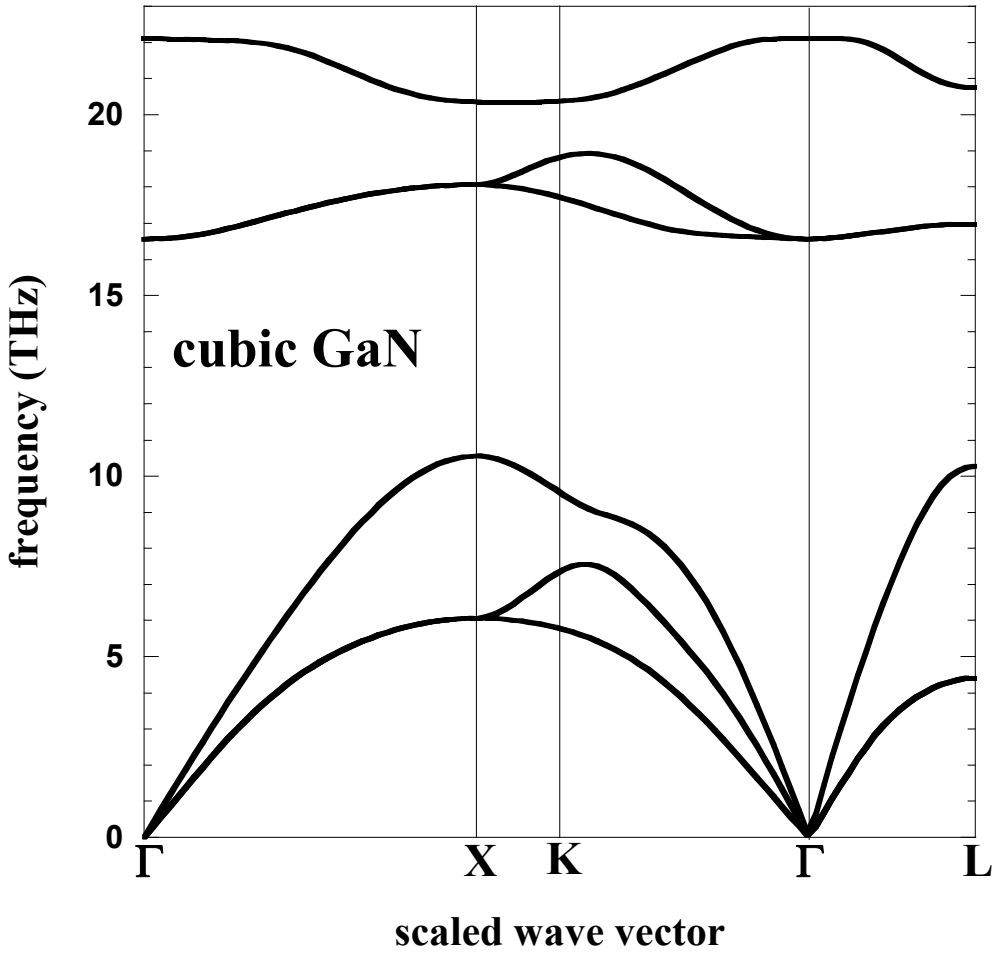

Figure A9

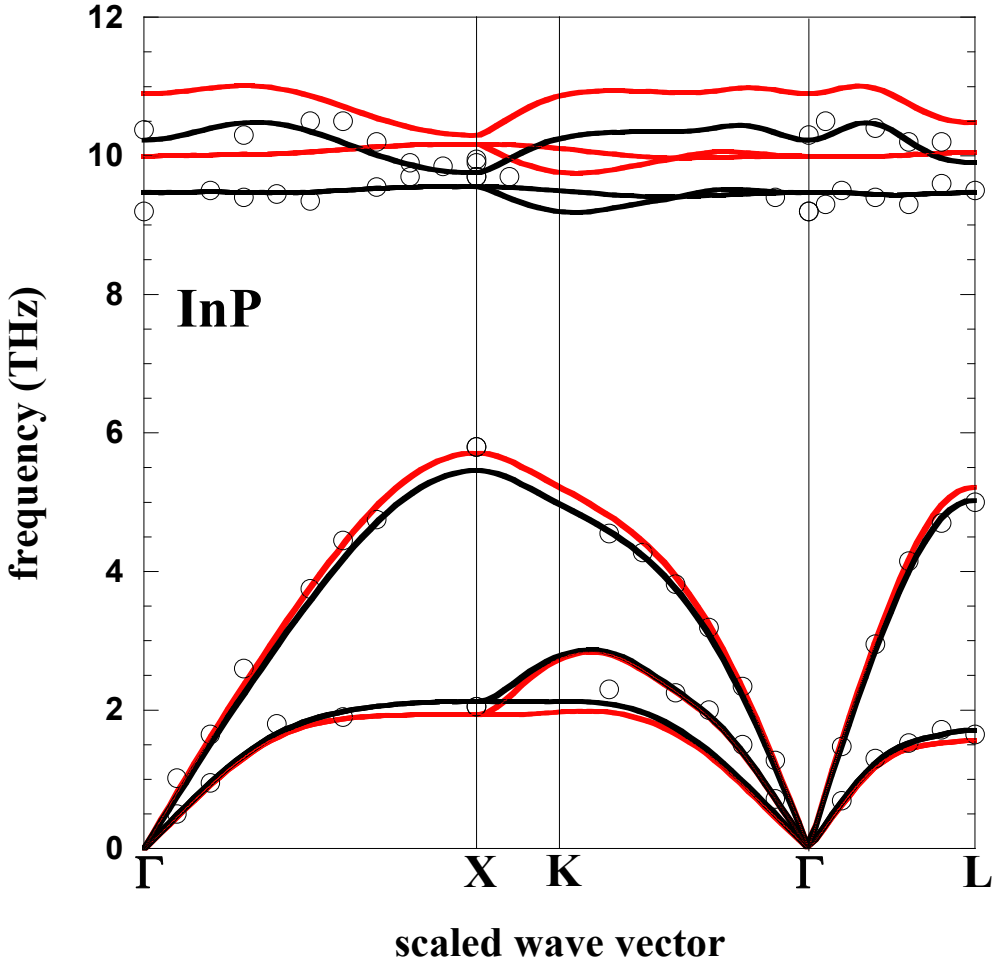

Figure A10

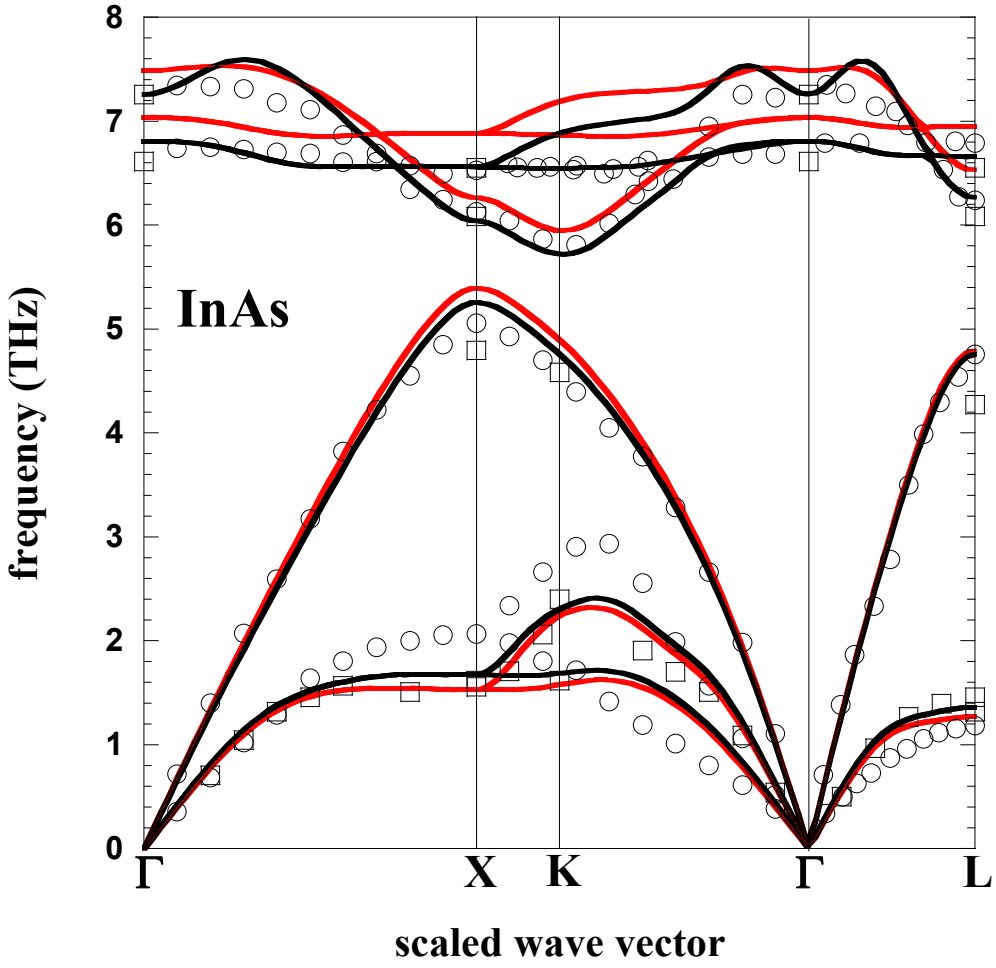

Figure A11

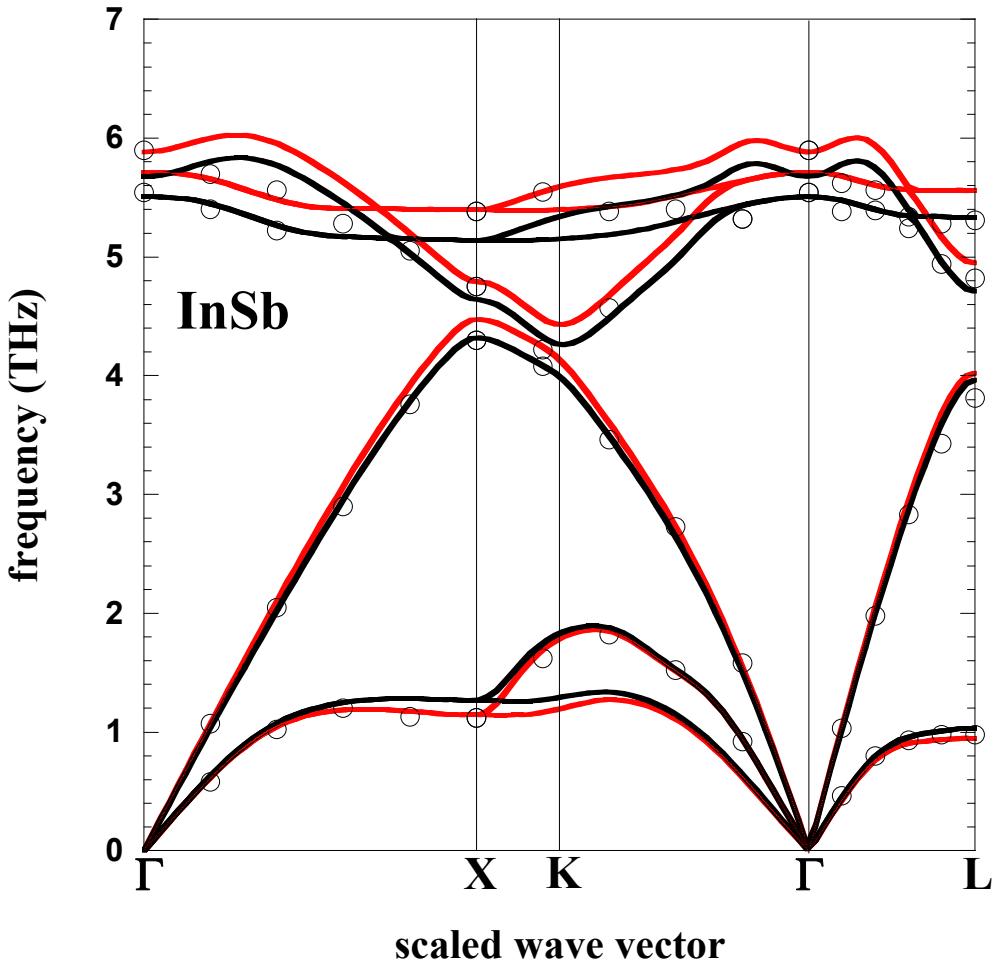

Figure A12

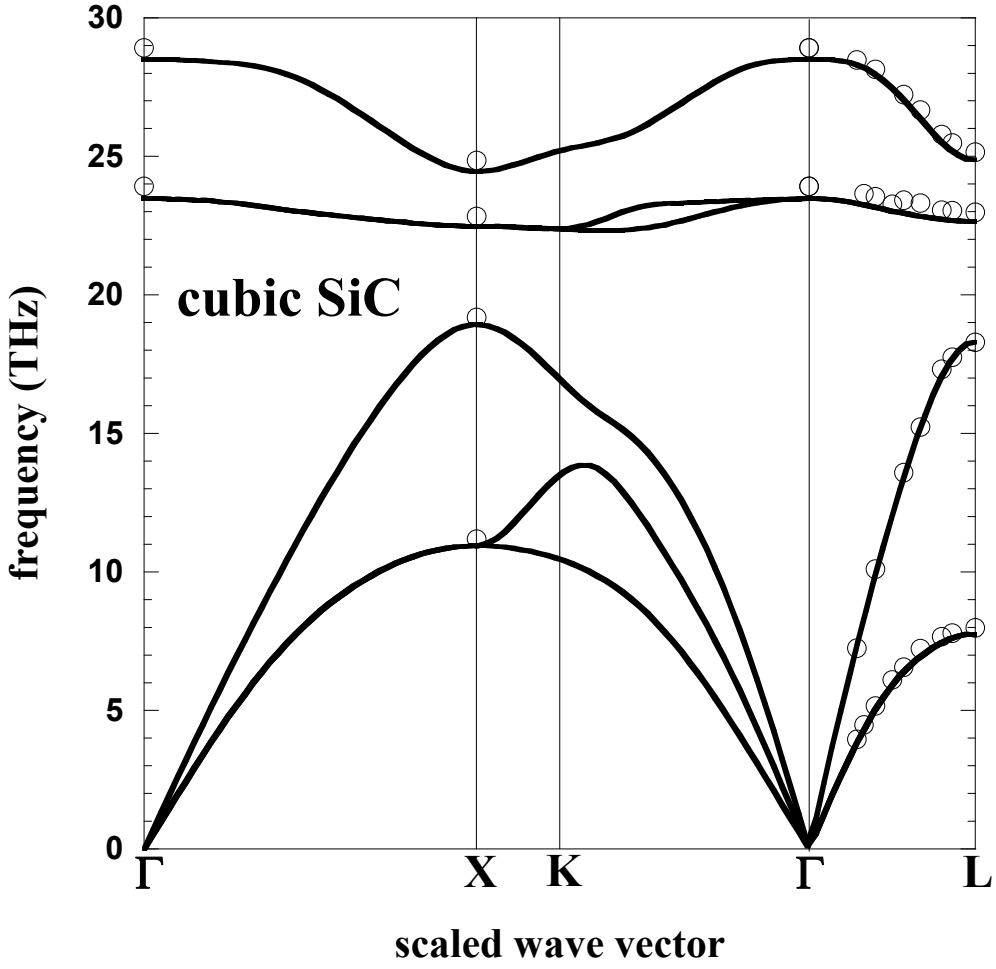
30
25
20
15
10
5
0
frequency (THz)
cubic SiC
Γ
X
K
Γ
L
scaled wave vector

Figure A13

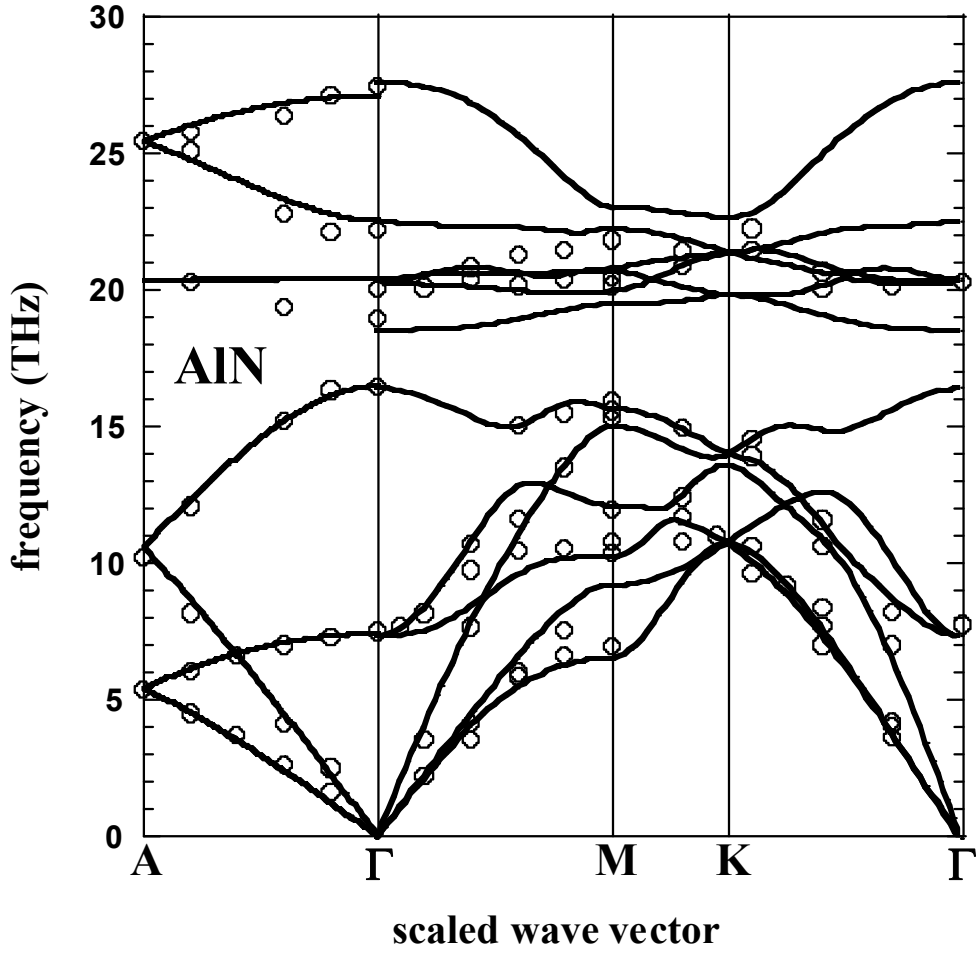

Figure A14